nature chemical biology

ARTICLES

https://doi.org/10.1038/s41589-020-0628-4

Structural basis for antibiotic action of the B_1 antivitamin 2′-methoxy-thiamine

Fabian Rabe von Pappenheim[1,2,5], Matteo Aldeghi[3,5], Brateen Shome[4], Tadhg Begley[4], Bert L. de Groot[3]✉ and Kai Tittmann[1,2]✉

The natural antivitamin 2′-methoxy-thiamine (MTh) is implicated in the suppression of microbial growth. However, its mode of action and enzyme-selective inhibition mechanism have remained elusive. Intriguingly, MTh inhibits some thiamine diphosphate (ThDP) enzymes, while being coenzymatically active in others. Here we report the strong inhibition of *Escherichia coli* transketolase activity by MTh and unravel its mode of action and the structural basis thereof. The unique 2′-methoxy group of MTh diphosphate (MThDP) clashes with a canonical glutamate required for cofactor activation in ThDP-dependent enzymes. This glutamate is forced into a stable, anticatalytic low-barrier hydrogen bond with a neighboring glutamate, disrupting cofactor activation. Molecular dynamics simulations of transketolases and other ThDP enzymes identify active-site flexibility and the topology of the cofactor-binding locale as key determinants for enzyme-selective inhibition. Human enzymes either retain enzymatic activity with MThDP or preferentially bind authentic ThDP over MThDP, while core bacterial metabolic enzymes are inhibited, demonstrating therapeutic potential.

As we enter an era of antibiotic scarcity[1], the discovery or development of new compounds with antibiotic properties is of great importance. Most antibiotics target either translation by inhibiting the ribosome or cell-wall biosynthesis[2]. As for previous generations of antibiotics, which were often derived from naturally occurring precursors, nature may serve as a source of inspiration and a springboard for the development of new classes of antibiotics. While substrate analogs targeting housekeeping enzymes have been used for decades as antibiotics, less attention has been paid to the potential pharmaceutical application of naturally occurring vitamin analogs. Currently, three naturally occurring antivitamins have been described: (1) the riboflavin (vitamin B_2) analog roseoflavin (RoF)[3], (2) the pyridoxine (vitamin B_6) analog ginkgotoxin (GT)[4] and (3) the thiamine (vitamin B_1) analog MTh, which is derived from bacimethrin (4-amino-5-hydroxymethyl-2-methoxy-aminopyrimidine[5,6]; Extended Data Fig. 1). The design principles and general modus operandi of these antivitamins are highly similar as they all bear a small chemical modification of the vitamin scaffold, are taken up by the target species in the form of a modified precursor and are eventually transformed by the native downstream machinery responsible for biosynthesis of the biologically active cofactor form, often with higher affinity than the native cofactor, to yield the mature cofactor analog[6–11].

The toxic mode of GT is not fully understood, although it is clear that the methylation of pyridoxine at the functional C4′-OH position chemically inactivates the cofactor (Extended Data Fig. 1). Cumulative evidence strongly suggests that GT acts primarily by inhibiting pyridoxal 5′-phosphate biosynthesis but possibly also by replacing the genuine cofactor in pyridoxal 5′-phosphate enzymes with a chemically inert analog[8]. RoF was shown to inhibit the biosynthesis of flavin mononucleotide (FMN) and flavin adenine dinucleotide (FAD) at the genetic level by binding to a regulatory riboswitch, effectively suppressing transcription of FMN biosynthetic enzymes (Extended Data Fig. 1)[9]. Also, RoF displaces FMN or FAD in some flavoenzymes in its matured cofactor form, reducing the enzymatic activity of those enzymes by virtue of its differing redox potential compared to genuine FMN or FAD[10].

In MTh, the 2′-methyl group of authentic thiamine is replaced by a methoxy function (Extended Data Fig. 1). Notably, the catalytic apparatus of thiamine is thus kept intact as both the reactive site, the thiazolium heterocycle as well as the co-catalytic aminopyrimidine, are not defunctionalized. Cellular studies indicated that neither the MTh precursor bacimethrin nor MTh itself nor the fully matured diphosphorylated MThDP cofactor affected the expression of thiamine biosynthetic genes or downstream cofactor maturation[6]. It was thus suggested that the antibiotic properties of MTh stem from inhibition of ThDP enzymes upon MThDP binding. A set of enzyme targets for MThDP was identified in *E. coli*, namely α-ketoglutarate dehydrogenase, transketolase (TK) and 1-deoxy-D-xylulose-5-phosphate synthase (DXS). In vitro studies on several ThDP enzymes demonstrated that the enzymatic activities of both *E. coli* pyruvate dehydrogenase (*Ec*PDH) and *E. coli* 1-deoxy-D-xylulose-5-phosphate synthase are strongly inhibited upon reconstitution with MThDP[11]. Conversely, *E. coli* α-ketoglutarate dehydrogenase and human PDH retain almost full enzymatic activity with MThDP as the cofactor[11]. This underscores the notion that MThDP is, in principle, coenzymatically active, but it remains unclear why only some ThDP enzymes are inhibited by MThDP. In the absence of structural information and mechanistic analyses, the mode of action of MThDP and its enzyme-selective inhibition have remained elusive.

Transketolase from *E. coli* (*Ec*TK) forms a functional dimer with two active sites harboring the ThDP cofactor at the monomer–monomer interface and catalyzes in vivo the transfer of two-carbon (C2) units between phosphoketoses and phosphoaldoses (Fig. 1 and Extended Data Fig. 2)[12,13]. The two active sites are linked through a proton wire that consists of six glutamate residues (three contributed

[1]Department of Molecular Enzymology, Göttingen Center of Molecular Biosciences, University of Göttingen, Göttingen, Germany. [2]Department of Structural Dynamics, Max Planck Institute for Biophysical Chemistry, Göttingen, Germany. [3]Research Group of Computational Biomolecular Dynamics, Max Planck Institute for Biophysical Chemistry, Göttingen, Germany. [4]Department of Chemistry, Texas A&M University, College Station, TX, USA. [5]These authors contributed equally: Fabian Rabe von Pappenheim, Matteo Aldeghi. ✉e-mail: bgroot@gwdg.de; ktittma@gwdg.de

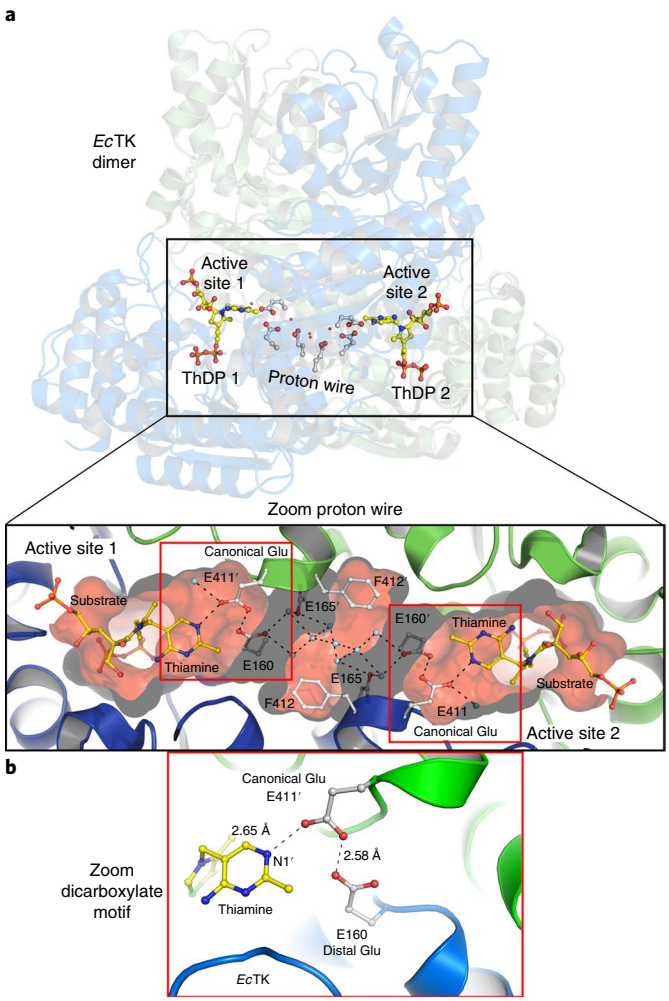

Fig. 1 | Structure of the *Ec*TK dimer and communication proton wire. **a**, Structure of the *Ec*TK dimer showing the two active sites with bound ThDP cofactors at the monomer–monomer interface and the proton wire linking both active sites (2R8O)[17]. Lower panel: detailed view of the proton wire showing residues 411′-E160-E165′-(twofold symmetry axis)-E165-E160′-E411 as well as water molecules (cyan spheres) and the cofactor aminopyrimidine. Residues contributed by monomer B are marked with an apostrophe. Note that Glu411 is a canonical residue in ThDP enzymes required for cofactor activation. **b**, Glu411 also forms a hydrogen bond with a second, distal glutamate (Glu160; red boxes). The corresponding dicarboxylate in *Hs*TK was shown to form transient LBHBs as critical switching elements for cooperativity signaling through the proton wire[14].

by each monomer: Glu411, Glu160 and Glu165) and several bridging water molecules (Fig. 1a). The wire is thought to synchronize catalysis in the dimer by reversibly shuttling a proton involving transient low-barrier hydrogen bonds (LBHBs)[14,15]. These LBHBs are formed between a canonical glutamate (Glu411 in *Ec*TK) that chemically activates ThDP through protonation at the N1′ atom and a neighboring, distal glutamate of the proton wire (Glu160; Fig. 1b). Notably, the proton wire, including the dicarboxylate motif, is conserved in all TKs[14]. Reciprocal cofactor activation in the *Ec*TK dimer is thought to proceed by Glu411-catalyzed protonation of ThDP N1′, tautomerization of the ThDP aminopyrimidine to the corresponding imino tautomer and acid–base catalysis of the latter (intramolecularly or via a water molecule) to form the reactive thiazolium carbene/carbanion, which in turn attacks the substrate (Extended Data Fig. 2b)[14–18].

Here, we combine kinetic and thermodynamic analyses of binding and catalysis with ultrahigh-resolution X-ray crystallography and molecular dynamics (MD) simulations to unravel the molecular mode of action of MThDP and the basis of enzyme-selective inhibition in the ThDP enzyme family. Our study pinpoints the realistic potential of the MTh antivitamin for antibiotic treatment.

Results

Catalytic competence of *Ec*TK with MThDP. To initially gauge the coenzymatic activity of MThDP bound to *Ec*TK, we conducted steady-state kinetic experiments using the physiological substrates (X5P) and D-ribose-5-phosphate (R5P; Fig. 2a). This analysis revealed that catalytic turnover (k_{cat}) was greatly reduced in *Ec*TK reconstituted with MThDP ($k_{cat} = 1.9 \pm 0.1\,s^{-1}$; 3.7% residual activity) compared to *Ec*TK with authentic ThDP as the reference ($k_{cat} = 51.3 \pm 0.4\,s^{-1}$), while the substrate affinity (K_M^{app}) for donor X5P was almost identical (Fig. 2a and Supplementary Table 1). The binding affinity of *Ec*TK toward MThDP ($K_D^{app} = 21.9 \pm 2.2\,\mu M$) under steady-state turnover conditions was approximately tenfold lower than ThDP ($K_D^{app} = 2.0 \pm 0.2\,\mu M$) translating into a thermodynamic penalty of ~1.3 kcal mol^{-1} (Fig. 2a). Similar results were obtained by fluorescence-based cofactor titration experiments using the static quenching of protein fluorescence accompanied by cofactor binding, although two different binding regimes were detected in this case (Extended Data Fig. 3a). In contrast to genuine ThDP, MThDP did not give rise to the typical near-ultraviolet (UV) circular dichroism (CD) and absorbance charge-transfer bands when bound to *Ec*TK, alluding to a slightly different binding mode (Extended Data Fig. 3b)[19,20].

To identify the kinetic bottleneck of the greatly reduced turnover in *Ec*TK with bound MThDP, we analyzed the quantitative distribution of *Ec*TK reaction intermediates by chemical quench/^{1}H-NMR spectroscopy (Fig. 2b)[17,21,22]. This method detects key catalytic intermediates, making it a diagnostic tool for assessing rate-limiting steps. In the case of *Ec*TK with genuine ThDP, the covalent substrate–ThDP conjugate is accumulated under steady-state conditions[17]. In stark contrast, C2-unreacted cofactor was detected as a major intermediate for *Ec*TK with bound MThDP (Fig. 2b). This altered intermediate distribution along with the reduced k_{cat} suggests a change in the rate-limiting step of *Ec*TK reconstituted with MThDP. Since substrate affinity (K_M^{app}) was virtually unchanged, this implies a reduced reactivity of bound MThDP, presumably through impaired cofactor activation. To test whether cofactor activation had indeed become rate limiting in *Ec*TK with MThDP, we measured the solvent hydrogen–deuterium (H/D) exchange at C2 of *Ec*TK-bound MThDP versus *Ec*TK with genuine ThDP (Fig. 2a)[16]. In the latter, k_{obs} amounted to $313 \pm 41\,s^{-1}$, demonstrating that cofactor activation was not rate limiting for *Ec*TK catalysis ($k_{cat} = 53\,s^{-1}$). However, H/D exchange at C2 of MThDP bound to *Ec*TK proceeded two orders of magnitude slower ($k_{obs} = 2.9 \pm 1.1\,s^{-1}$) and disclosed a rate-limiting cofactor activation for overall turnover ($k_{cat} = 1.8 \pm 0.1\,s^{-1}$).

Structural basis of *Ec*TK inhibition by MThDP. To gain structural insights into the binding mode of MThDP in *Ec*TK and to decipher the structural basis of the reduced coenzymatic activity, including the impaired cofactor activation and reduced binding affinity of the antivitamin, we crystallized *Ec*TK in complex with MThDP and determined the X-ray crystallographic structure of the holoenzyme at sub-ångstrøm resolution of 0.92 Å (Fig. 3 and Supplementary Table 2). All parts of enzyme-bound MThDP, including the unique 2′-methoxy functional group, exhibited well-defined electron density, providing the basis for a reliable structural model (Fig. 3a). While MThDP adopted the classic V-shaped conformation of the

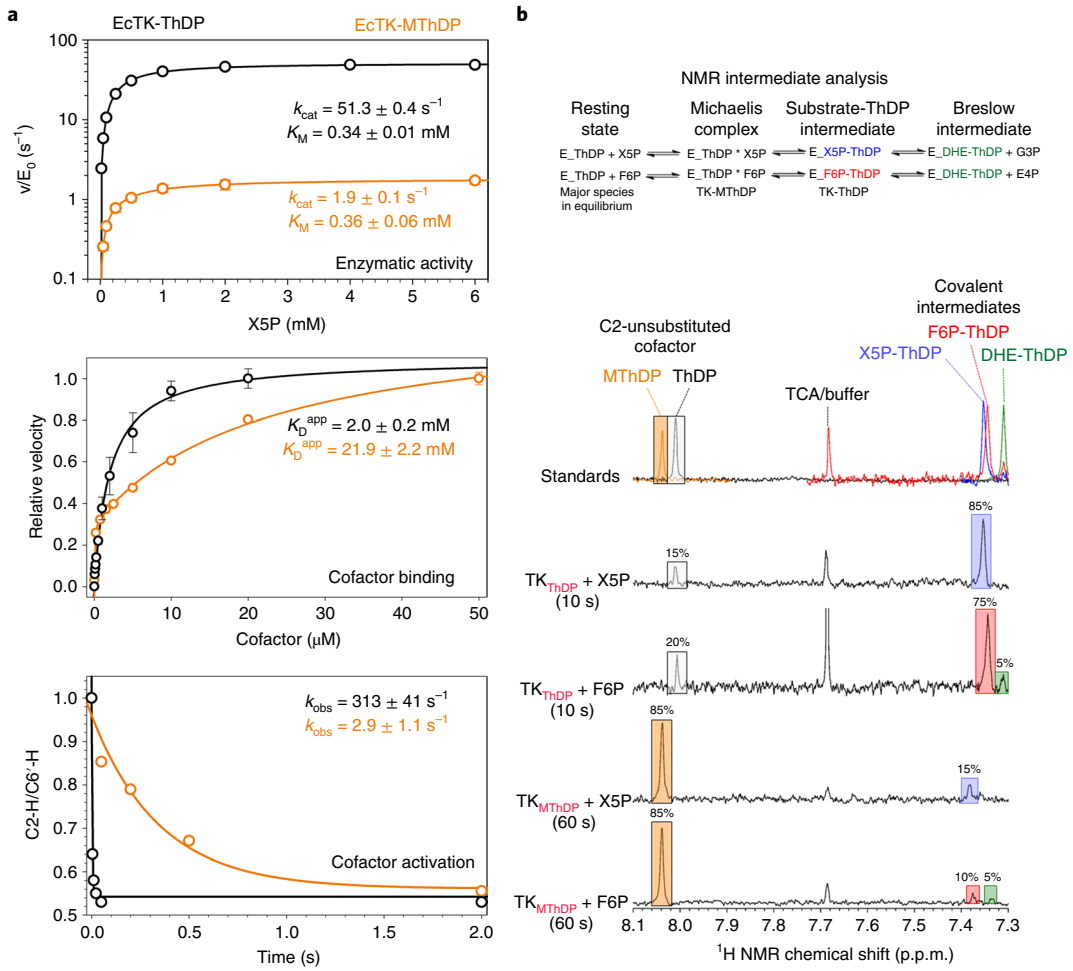

Fig. 2 | Functional characterization of *Ec*TK reconstituted with genuine ThDP versus antivitamin-derived MThDP. a, Graphs showing the analysis of enzymatic activity, cofactor binding and cofactor activation. Top: steady-state kinetic analysis of enzymatic activity for the conversion of physiological substrates X5P and R5P revealed a greatly reduced overall activity (k_{cat}) for the MThDP-reconstituted enzyme (orange) but an unchanged substrate affinity (K_M^{app}) for X5P. Note the logarithmic scale for the measured rates. Middle: analysis of cofactor binding under steady-state turnover conditions revealed a tenfold reduced affinity of *Ec*TK for MThDP compared to ThDP (black). Bottom: cofactor activation as measured by H/D exchange at the C2 position of enzyme-bound cofactor highlighted a 100-fold reduction of the pseudo-first-order rate constant for MThDP relative to genuine ThDP. The almost identical value of the observed rate constant (2.9 s^{-1}) and k_{cat} (1.9 s^{-1}; top) suggest that cofactor activation is rate limiting for overall catalysis in *Ec*TK with bound MThDP. All kinetic and thermodynamic constants are provided in Supplementary Table 1. All measurements were carried out in triplicate and are shown as the mean ± s.d. **b**, Quantitative analysis of reaction intermediates of the *Ec*TK donor substrate half-reaction by chemical quench/^{1}H-NMR spectroscopy. Top: schematic of the TK donor half-reaction showing key intermediates and associated chemical equilibria. The main accumulated species in equilibrium are indicated for *Ec*TK reconstituted with either genuine ThDP or antivitamin-derived MThDP. DHE, 1,2-dihydroxylethyl. Bottom: intermediate distribution of reaction intermediates by ^{1}H-NMR spectroscopy isolated by acid quenching from *Ec*TK and reconstituted with either ThDP or MThDP after reaction with donor ketose substrates X5P and F6P. Note the dominant accumulation of the covalent X5P-ThDP and F6P-ThDP intermediates in the case of the TK complex with genuine ThDP as cofactor, while C2-unsubstituted MThDP was observed as a major species for TK with MThDP despite adding saturating amounts of donor substrate. This observation indicates that carbonyl addition of donor substrates to enzyme-bound MThDP is defective, leading to accumulation of the non-covalent substrate–enzyme Michaelis complex.

thiazolium and aminopyrimidine heterocycles as observed for genuine ThDP[23], its binding mode and interactions with protein groups were somewhat different. Notably, the 2′-methoxy group (2′-methyl in ThDP), which is in plane with the aminopyrimidine ring, pointed toward and clashed into the sidechain of the canonical, cofactor-activating Glu411 (refs. [23,24]) and disengaged the latter from hydrogen bonding with N1′ of the MThDP aminopyrimidine (Fig. 3b). Instead, Glu411 seemingly formed a short LBHB with neighboring residue Glu160 (O-O interatomic distance, 2.49 Å) as indicated by both the 2mFo-DFc electron density map and the mFo-DFc difference electron density map (centrally localized density between Glu411′ and Glu160 suggests a hydrogen in equidistant position; Fig. 3b). These structural observations rationalize the detected defunctionalized cofactor activation in *Ec*TK with MThDP (see above) as well as the lower binding affinity that apparently results from a steric clash of the 2′-methoxy group with the sidechain of Glu411′. A structural comparison of MThDP versus genuine ThDP when bound to *Ec*TK showed that the aminopyrimidine of MThDP was displaced by approximately 1 Å relative to that of ThDP, resulting in its aforementioned disconnection from the catalytically essential Glu411, abrogating cofactor activation (Fig. 3c). At the same time, the interaction between the two LBHB-forming residues

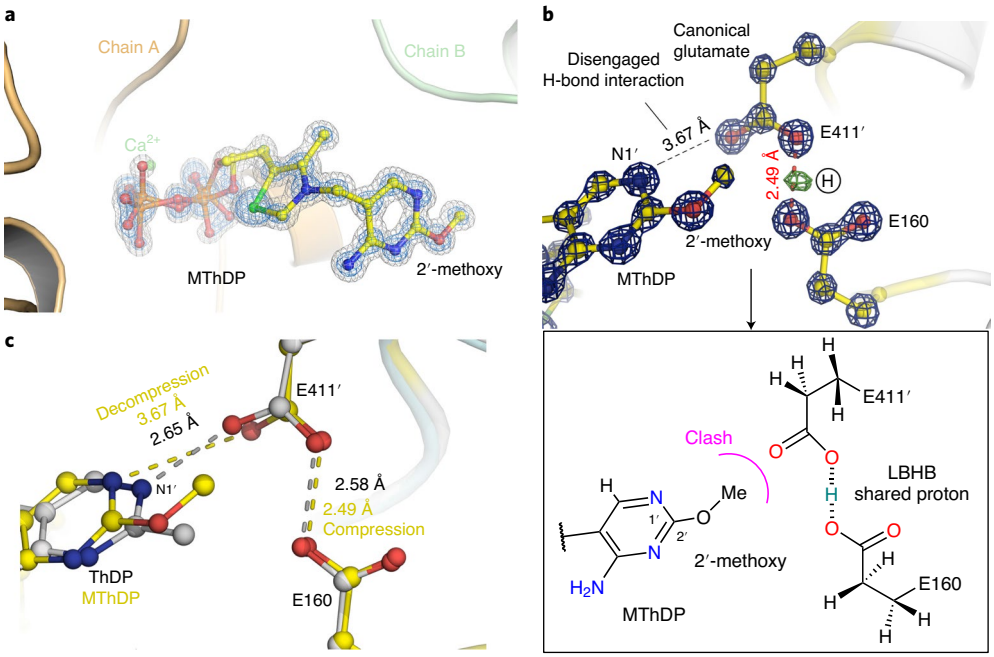

Fig. 3 | Structure of *Ec*TK in complex with 2′-methoxy-ThDP at 0.92 Å resolution. a, Simulated annealing mFo-DFc omit electron density map of the MThDP cofactor bound to *Ec*TK shown at contour levels of 10σ (blue) and 7σ (gray). The unique 2′-methoxy function is labeled. Note the structural flexibility of the diphosphate portion of MThDP. The two chains of the homodimer (A and B) are colored individually. **b**, Structure of enzyme-bound MThDP showing the cofactor aminopyrimidine portion including the unique 2′-methoxy function, the canonical Glu411′ and the distal Glu160. The structural model is superposed with the corresponding 2mFo-DFc electron density map (blue) displayed at a contour level of 2.7σ. We observed extra electron density in the mFo-DFc difference electron density map between the two glutamates (green; contour level, 3.5σ), indicating the presence of a shared hydrogen in a LBHB interaction. Interatomic distances are shown for the interaction between cofactor N1′ and Glu411′, as well as for the glutamates. Note the long interatomic distance between the cofactor and Glu411′ resulting from the steric clash of the 2′-methoxy group into Glu411′. **c**, Superposition of *Ec*TK with bound MThDP (yellow; this study) versus *Ec*TK with authentic ThDP (gray; 2R8O). Bond lengths of critical hydrogen-bonding interactions are provided. Note the marked displacement of the aminopyrimidine portion and the compressed interaction between Glu411′ and Glu160 in the MThDP-reconstituted enzyme. Crystallographic statistics are provided in Supplementary Table 2.

Glu411 and Glu160 was further compressed, indicating a strengthened hydrogen-bonding interaction, which we consider as 'anticatalytic', since the essential residue 411 is 'trapped' in this interaction.

We next examined the reaction of *Ec*TK with MThDP and substrate X5P in crystallo. Given our aforementioned functional and structural findings, we predicted that no covalent intermediate between cofactor and substrate would be formed to a detectable extent, as was observed for *Ec*TK with genuine ThDP. Thus, we soaked *Ec*TK-MThDP crystals with high concentrations of substrate X5P, flash cooled the crystals and determined the structure of the enzyme–substrate complex at a resolution of 0.95 Å (Supplementary Table 2). The binding locale and conformation of bound X5P could be unambiguously traced in the electron density maps, which were of high quality, and allowed a reliable modeling of X5P in the reactive keto form (Fig. 4 and Extended Data Fig. 4a). X5P was found, as expected, to bind non-covalently (Michaelis complex) to the active site and was accommodated atop the thiazolium moiety of MThDP. The position and conformation of X5P would not allow an immediate reaction with the cofactor due to a relatively long interatomic C-C distance (~4 Å) between the reactive MThDP C2 atom and the X5P carbonyl carbon and a highly unfavorable orientation of X5P with respect to the preferred Burgi–Dunitz trajectory of carbonyl additions (attacking angle of thiazolium C2 toward X5P carbonyl was ~40° instead of the optimal 107°; Fig. 4c)[25]. We would hence classify this binding mode as a pre-reaction mode rather than a near-attack mode. X5P was firmly held in place by numerous hydrogen-bonding interactions with the protein, the MThDP cofactor and water molecules (Fig. 4a,d). Analysis of bond lengths of bound X5P (Fig. 4b) indicated no apparent anomalies (that is, bond elongations or compressions), as were observed for the covalent substrate–ThDP conjugates, where the scissile substrate C2-C3 bond was selectively lengthened by 0.1 Å (at the given resolution and ligand B-factors, the coordinate error as judged by the estimated s.d. of the calculated bond lengths amounted to 0.01–0.02 Å)[26,27]. We thus concluded that the substrate was not yet stressed at this stage of the reaction. Akin to our observation for the resting-state enzyme, Glu411 and Glu160 formed a short LBHB (Fig. 4d), showing that this interaction was indeed anticatalytic, as it is kept through several stages of the catalytic cycle and trapped the catalytic key player Glu411 in a non-productive pairing with Glu160. A superposition of the active sites of *Ec*TK-MThDP with X5P in the pre-reaction state (this study) versus that of *Ec*TK-ThDP in covalent complex with X5P (ref. [17]; Fig. 4e and Extended Data Fig. 4b,c) illustrated that formation of the covalent substrate–cofactor conjugate is accompanied by a further movement of the substrate toward the cofactor thiazolium and a concomitant rotation by almost 180° around the substrate C2-C3 bond, which effectively led to a (+1) register shift of the hydrogen-bond interactions between protein and the substrate OH groups. As a consequence of this screw-like motion, the 1-OH group of X5P rotated away from the 4′-amino group of the cofactor to the opposite structural face and displaced a water molecule, while the 2-OH (previously carbonyl) occupied the position close to N4′. The 3-OH and 4-OH groups of X5P moved ~1.5 Å deeper into the active-site pocket without notable rotation. No major structural differences were observed for active-site residues in the two different catalytic states (Extended Data Fig. 4b,c).

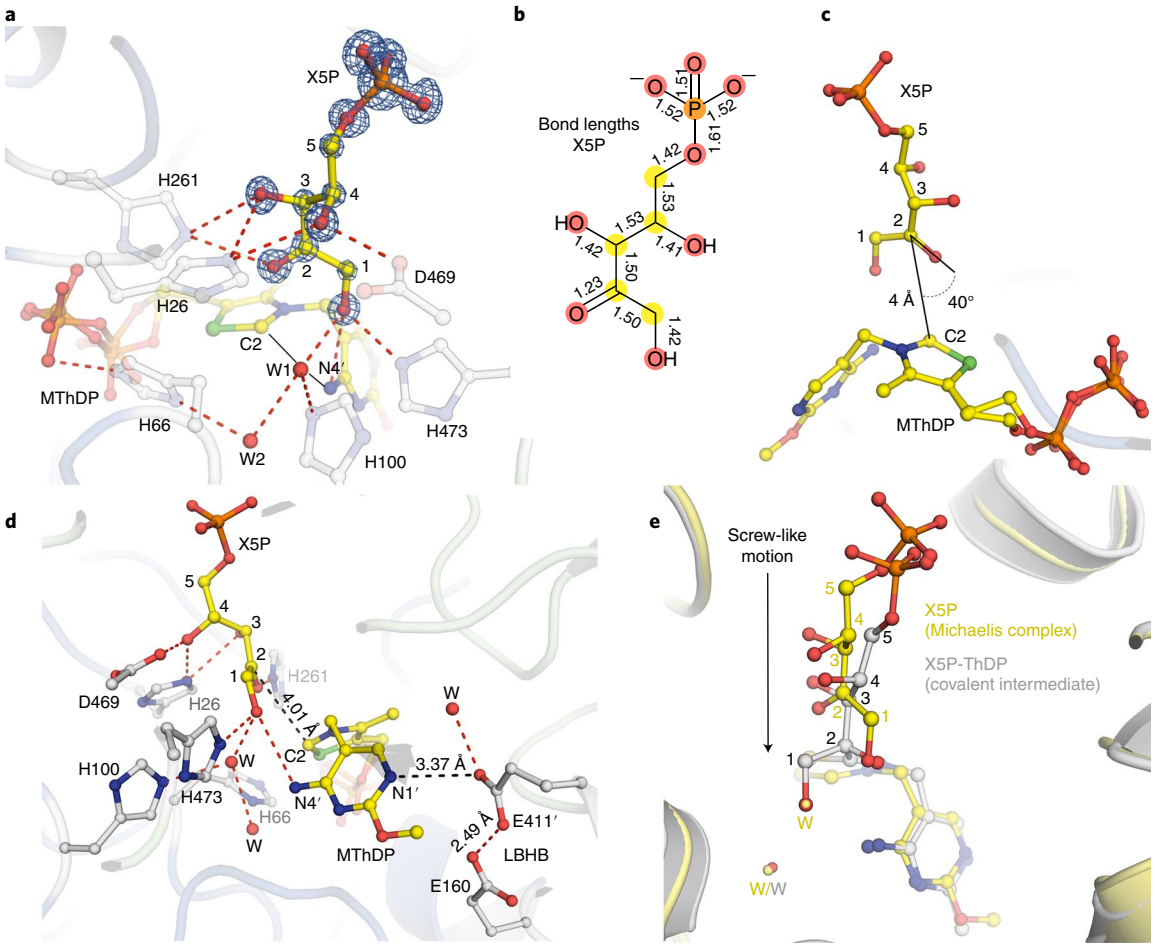

Fig. 4 | Structure of *Ec*TK with 2′-methoxy-ThDP and donor substrate X5P at a resolution of 0.95 Å. a, Structure of *Ec*TK in non-covalent complex with donor substrate X5P showing the final refined model of the bound substrate, selected active-site residues, the MThDP cofactor and water (W) molecules. The structural model of the bound substrate is superposed with the 2mFo-DFc omit electron density (blue) contoured at 2σ. The individual carbon atoms of X5P are labeled. **b**, Calculated bond lengths of bound substrate X5P. **c**, Relative orientation of the reactive 2′-methoxy-ThDP thiazolium moiety toward substrate X5P bound in a pre-reaction state Michaelis complex showing the interatomic distance between C2 of MThDP and the carbonyl C2 of X5P, as well as the attacking angle of the MThDP C2 point nucleophile onto the carbonyl group of X5P. Both distance and angle are not favorable according to the preferred Burgi–Dunitz trajectory[25]. **d**, Structure of the *Ec*TK Michaelis complex with donor substrate X5P showing the active site with cofactor, substrate, protein groups and water molecules. Cofactor MThDP and substrate X5P are highlighted in yellow; amino acid residues interacting with X5P and residues required for cofactor activation (Glu411′ and Glu160) are shown in gray. Hydrogen-bonding interactions are indicated by red dashed lines. Note the compressed interaction between Glu411′ and Glu160 and the disengaged hydrogen bond between the cofactor N1′ atom and Glu411′. **e**, Superposition of the structures of *Ec*TK in non-covalent Michaelis complex (this study) and in covalent complex (2R8O)[17] with substrate X5P. The individual atoms of the carbon skeleton are labeled. During the addition of the substrate carbonyl to the cofactor, substrate X5P underwent a screw-like motion with a 180° rotation around the C2-C3 bond accompanied by substrate penetration. Crystallographic statistics are provided in Supplementary Table 2. Simulated annealing omit maps for X5P and stereo views of *Ec*TK in non-covalent and covalent complex with X5P are shown in Extended Data Fig. 4.

The structural basis of enzyme-selective inhibition by MThDP. Our findings underline the critical importance of proton transfers required for cofactor activation, as a misalignment impairs cofactor protonation by the canonical glutamate[16] (here Glu411), resulting in the greatly reduced activation rate observed. However, this implies that some ThDP-dependent enzymes, namely those previously demonstrated to be almost fully active with MThDP[11], are able somehow to meet the steric requirements of the modified cofactor while keeping the catalytic apparatus intact. Thus, we set out to compare different key metabolic ThDP enzymes with either greatly reduced or retained activity when binding MThDP, focusing on the human and corresponding *E. coli* enzymes to explore the potential of MTh for antibiotic treatment. Within the scope of this study, we included *Ec*TK and *Ec*PDH, and the corresponding human orthologs *Hs*TK and *Hs*PDH. Our analyses and research by others have shown that the two *E. coli* enzymes are strongly inhibited by MThDP, while the *Hs*PDH retains almost full activity (Supplementary Table 3)[11]. *Hs*TK has not yet been studied in that regard.

To close this gap of knowledge, we analyzed the activity of *Hs*TK in the presence of MThDP. *Hs*TK is unique among TKs in terms of cofactor binding, as binding of ThDP proceeds in a 'quasi-irreversible' manner and results from a structural isomerization during holoenzyme formation[28,29]. We produced recombinant *Hs*TK[29] and tested the enzymatic activity of the purified holoenzyme in the presence of a large molar excess (100 µM) of either MThDP or authentic ThDP as the reference for up to 24 h of incubation. No substantial loss of activity could be detected in these measurements (holo-*Hs*TK with excess ThDP: $k_{cat} = 2.35 \pm 0.07\ s^{-1}$; holo-*Hs*TK with excess MThDP: $k_{cat} = 2.27 \pm 0.06\ s^{-1}$; triplicate mean ± s.d.) showing that *Hs*TK does not undergo cofactor exchange and thus retains full enzymatic

activity (Supplementary Table 3). Next, we produced *Hs*TK apoenzyme and tested its enzymatic activity upon reconstitution with MThDP. The residual activity of *Hs*TK-MThDP ($k_{cat} = 0.05 \pm 0.01\ s^{-1}$) was at the detection limit of the spectrophotometric assay at ~3% compared to the residual activity of *Hs*TK-ThDP ($k_{cat} = 1.67 \pm 0.02\ s^{-1}$). It is unclear whether this low activity resulted from improper binding of MThDP or, alternatively, from defunctionalization of the cofactor activation apparatus, since the proton wires of *HsTK* and *Ec*TK are conserved (Extended Data Fig. 5). Near-UV CD spectra of *Hs*TK reconstituted with either MThDP or ThDP revealed similar results to those observed for *Ec*TK: MThDP did not give rise to the prominent band at 325 nm as authentic ThDP suggesting a different binding mode of MThDP (Fig. 5). Interestingly, when we added ThDP to holo-*Hs*TK-MThDP, we noticed a partial recovery of enzymatic activity over time, showcasing reversible binding of MThDP as opposed to quasi-irreversible binding of ThDP and that genuine ThDP outcompeted MThDP with respect to binding. The same implications could be derived by analyses of the recombination kinetics of *Hs*TK apoenzyme with ThDP in the absence or presence of MThDP in equimolar concentration: the recombination half-times and steady-state activities upon reconstitution were similar for both experiments, demonstrating that *Hs*TK effectively discriminated between ThDP and MThDP (Fig. 5e). In this regard, *Hs*TK resembles human and *E. coli* oxoglutarate dehydrogenase, which have been reported to keep almost full enzymatic activity in the presence of excess MThDP[11].

A structural comparison of the four enzymes (Fig. 5a–d) highlights that the cofactor methyl group of the two bacterial enzymes and of *Hs*TK points toward the catalytically essential dicarboxylate motif, while this is not the case in *Hs*PDH because the topology of the cofactor-binding pocket is different. In addition, while *Hs*TK, *Ec*TK and *Ec*PDH feature an acidic proton wire with a direct proton-transfer pathway between the two active sites, the putative wire in *Hs*PDH is structured differently, such as with replacements of wire glutamates by glutamines, suggesting a different atomistic mechanism of cooperativity as compared to bacterial enzymes (Extended Data Fig. 5)[15,30].

To gain further structural and in turn mechanistic insights into the differential inhibitory activity of MThDP between *E. coli* and human enzymes, we performed MD simulations (Supplementary Data). Different MD protocols were validated by comparing calculated binding free energies (ΔG) against experimental ones, and the computed data producing the closest agreement with experiment data were used for further analysis. The results shown here were obtained from 500 simulations that started from X-ray structures of ThDP-bound enzymes, during which ThDP was transformed into MThDP in 100 ps. This non-equilibrium approach returned binding-affinity changes between ThDP and MThDP that closely matched experimental data (Supplementary Table 4 and Extended

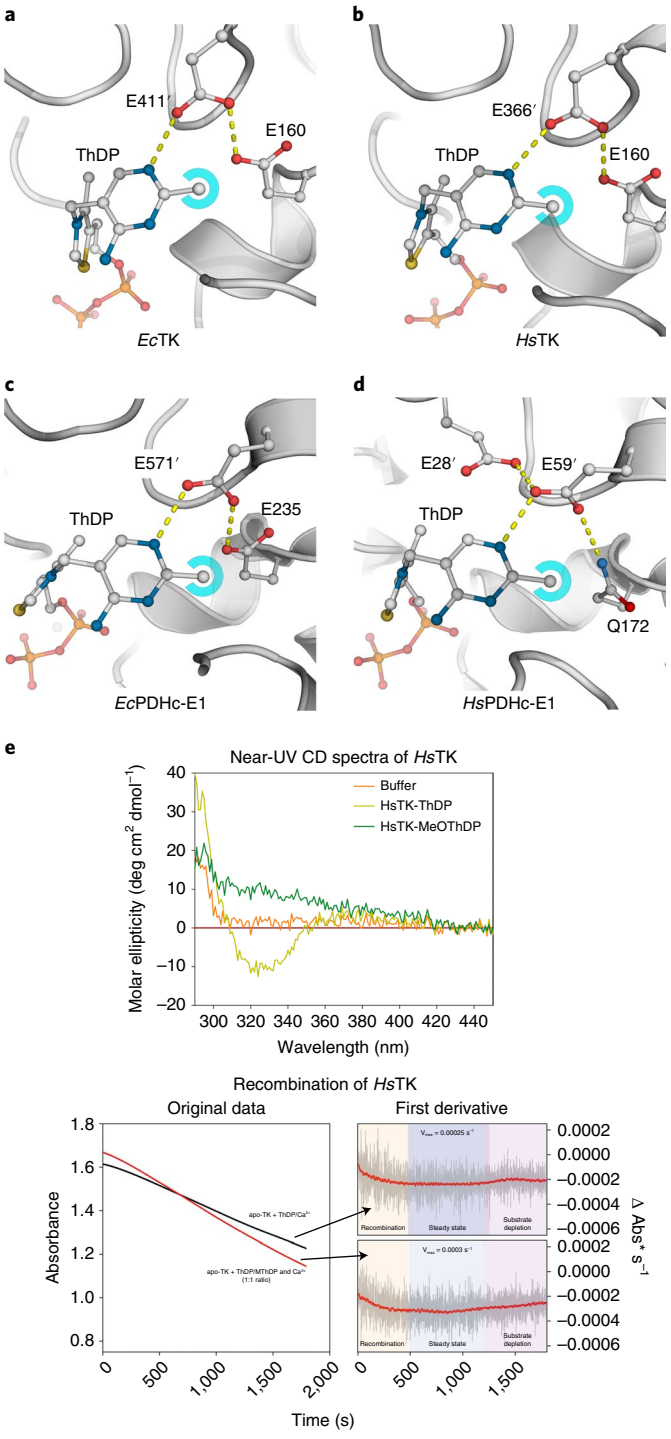

Fig. 5 | Cofactor-binding locale of *E. coli* and human ThDP enzymes and catalytic competence of *Hs*TK with 2′-methoxy-ThDP. a–d, Cofactor-binding motifs in *Ec*TK (**a**), *Hs*TK (**b**), *Ec*PDH E1 component (*Ec*PDHc-E1) (**c**) and human PDH E1 component (*Hs*PDHc-E1) (**d**); each showing the cofactor aminopyrimidine portions, the canonical glutamate required for cofactor activation and the second, distal glutamate interacting with the canonical glutamate. Putative hydrogen-bonding interactions are highlighted. The binding locale of the ThDP 2′-methyl group is highlighted (cyan) to illustrate the expected binding region of the unique 2′-methoxy group of antivitamin-derived MThDP. Note that the topology of the active site in *Hs*PDHc-E1 regarding the position of the distal glutamate (Glu28′) is different compared to the other enzymes. The following Protein Data Bank (PDB) codes were used: 1QGD for *Ec*TK; 3MOS for *Hs*TK; 2IEA for *Ec*PDH; and 3EXE for *Hs*PDH. **e**, Reconstitution of human TK apoenzyme with 2′-methoxy-ThDP and genuine ThDP. Top: Near-UV CD spectra of *Hs*TK after reconstitution of the apoenzyme with either genuine ThDP (yellow) or MThDP (green). Note the prominent CD signal with a negative signature at ~325 nm for *Hs*TK in complex with ThDP, which is absent for the enzyme complex with MThDP thus implying a different binding mode of MThDP. Bottom: Activity-based progress curves of cofactor recombination of *Hs*TK with either genuine ThDP and Ca^{2+} (black) or an equimolar mixture of ThDP and MThDP with Ca^{2+} (red) showing both the original data (left) and the first derivatives (right). The almost identical steady-state activities and time courses of recombination for both samples indicate that ThDP outcompetes MThDP in the recombination process. Experimental conditions are detailed in the Methods.

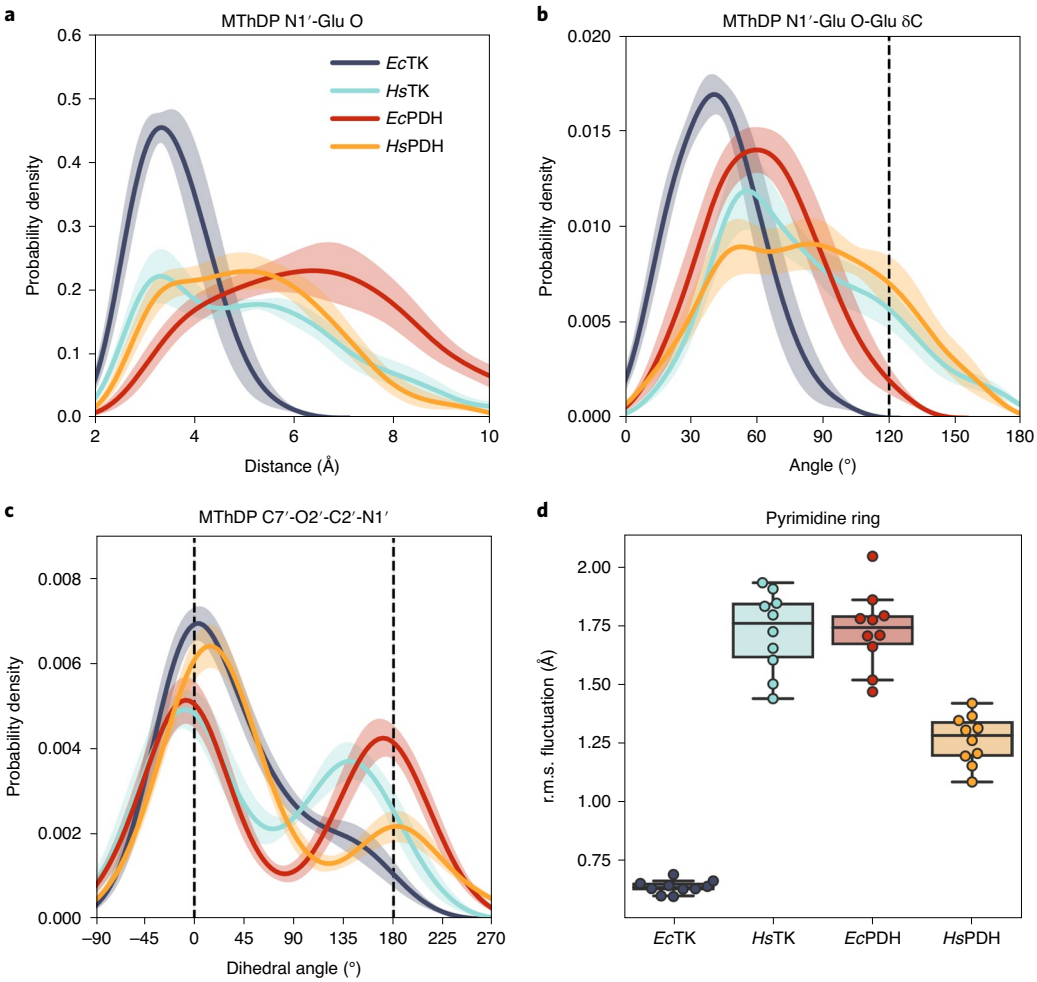

Fig. 6 | Distributions of TK-bound MThDP geometries obtained by MD simulations. a, Distributions for the interatomic distance between the N1′ atom of MThDP and the interacting oxygen of the canonical Glu residue donating the proton (Glu411 in *Ec*TK, 1QGD; Glu366 in *Hs*TK, 3MOS; Glu571 in *Ec*PDH, 2IEA; Glu59 in *Hs*PDH, 3EXE). **b**, Distributions for the angle between N1′ in MThDP, the oxygen and the δ-carbon of the canonical Glu residue. The dashed line indicates the ideal angle for proton transfers (120°). **c**, Distributions of the dihedral angle in MThDP involving the carbon and oxygen atoms of the 2′-methoxy group, the C2′ carbon and the N1′ nitrogen. Note that the 2′-methoxy function preferentially adopts a coplanar conformation relative to the aminopyrimidine ring, either 0° or 180°, as indicated by dashed lines. At a dihedral angle of 0°, the methoxy group points toward the canonical Glu (anti with 4′-amino group), while at a dihedral angle of 180°, it points to the opposite structural face (syn with 4′-amino group). **d**, Distributions of the average r.m.s. fluctuation values for the atoms in the pyrimidine ring of MThDP bound to the four enzymes studied. In **a**–**c**, solid lines represent the mean and the shaded area indicates the s.e. of the kernel density estimate across ten simulations. In **d**, the average r.m.s. fluctuation values for each of the $n = 10$ independent simulations are shown as a swarm plot, and the box plots are derived from these $n = 10$ average r.m.s. fluctuation values. The centers of the boxes indicate the median, the bounds of the boxes indicate the first and third quartiles of the distributions and the whiskers extend to 1.5 times the interquartile range. Samples outside the marked extrema are classified as potential outliers.

Data Fig. 6a–d). We thus proceeded to analyze the distribution of MThDP geometries obtained from these simulations. Because these simulations did not generate an equilibrium ensemble of conformations despite reporting on equilibrium free-energy differences[31], we limit our discussion to qualitative trends.

Figure 6a,b shows the distances and angles between the proton donor (oxygen of canonical glutamate) and acceptor (cofactor aminopyrimidine N1′) atoms for *Ec*TK, *Hs*TK, *Ec*PDH and *Hs*PDH. We assumed these would be correlated with the rate of cofactor activation and thus enzymatic activity. The insertion of the 2′-methoxy group in ThDP resulted in a broad distribution of donor–acceptor distances for all enzymes, with the notable exception of *Ec*TK (Fig. 6a). At the same time, in *Ec*TK, the 2′-methoxy group pointed toward the donating Glu411 (dihedral angle of zero; Fig. 6c) in most simulation snapshots. In addition, considering that the aminopyrimidine ring of MThDP did not deviate much from its average position (Fig. 6d), these observations suggest that the *Ec*TK-binding pocket could not easily accommodate the additional oxygen atom in MThDP, which is consistent with the loss of binding affinity of *Ec*TK toward MThDP as compared to genuine ThDP (Supplementary Tables 3 and 4). Similar trends emerged from the analysis of computed isotropic B-factors derived from the MD simulations (Extended Data Fig. 6e,f). The 2′-methoxy group was accommodated more easily in *Hs*TK, *Ec*PDH and *Hs*PDH. In fact, *Ec*PDH and *Hs*PDH were predicted to have similar affinities for ThDP and MThDP, while *Ec*TK seemed to thermodynamically discriminate between ThDP and MThDP (Supplementary Table 4). Given that the aminopyrimidine ring was allowed to move more substantially around its average position, together with a higher proportion of simulation frames in which the 2′-methoxy group oriented away from the canonical glutamate, suggests a higher plasticity of the binding pockets of these three enzymes (Fig. 6d). Notably, while *Hs*TK, *Ec*PDH and *Hs*PDH showed a broad

distribution of donor–acceptor distances (Fig. 6a), a higher fraction of the human homologs displayed optimal proton-transfer angles of ~120° (Fig. 6b). One might therefore speculate that the increase in donor–acceptor distance for MThDP as cofactor was compensated by a better geometry for proton transfers in the human enzymes, while this was not the case for the *E. coli* enzymes.

In addition to the above, we ran control simulations in which the 2′-methoxy group was not introduced into ThDP. These simulations showed that genuine ThDP had a higher fraction of potentially active donor–acceptor distances (<3 Å) than MThDP across all four enzymes tested (Extended Data Fig. 7a). However, the negative effect of the 2′-methoxy group was larger in the *E. coli* enzymes than the human ones. A weaker trend was observed for the donor–acceptor angles, where MThDP showed a similar distribution of angles toward the optimal angle as ThDP (Extended Data Fig. 7b).

Overall, our simulations point toward the subtle interplay between multiple dynamical variables, such as the fraction of optimal donor–acceptor distances and angles, as being responsible for the observed inhibitory ability of MThDP. This makes it difficult to confidently pinpoint a single mechanism that explains the differential effect of MThDP on *E.coli* and human enzymes. However, our experimental structural data together with the MD simulations pinpoint critical roles of the topology of the cofactor-binding site, in particular regarding the binding locale of the cofactor 2′-methoxy group relative to the canonical, cofactor-activating glutamate pairing with the second, distal glutamate of the proton wire, as well as the intrinsic plasticity of the cofactor-binding pocket.

Discussion

The experimental and computational results presented here provide a firm base for the origin of the toxic character of the thiamine (vitamin B_1) antivitamin MTh. In the latter, the cofactor methyl function is replaced by a methoxy group that is larger in size and exhibits a non-linear, angular arrangement of the atoms. When bound to *Ec*TK, a key enzyme of the pentose phosphate pathway, the 2′-methoxy function clashes into a canonical glutamate and disengages this residue from hydrogen bonding to the cofactor, impairing cofactor activation and thus catalysis. This catalytic glutamate is forced into a short, persistent LBHB with a neighboring glutamate of the signaling proton wire, both in the resting state and in complex with the substrate. This observation demonstrates that strong LBHBs in reactant states of enzyme catalysis can indeed be anticatalytic as proposed earlier[32,33] because they may freeze out overly stable, non-productive states by 'out-tuning' otherwise intimately coupled proton-transfer potentials[14]. Our recent studies in that field indicated that LBHBs are critical elements of cooperativity pathways in enzyme multimers but are not particularly stable to ensure rapid signaling in both directions of the wire[14].

Owing to the defunctionalized cofactor activation apparatus, we were able to determine the first structure of a TK in non-covalent complex with a donor ketose (here X5P). Substrate binding does not adhere to the principle of least motion[22], as the transition from the pre-reaction Michaelis complex to the covalent conjugate with the thiamine cofactor entails a complex screw-like motion of the substrate, with a concomitant +1 register shift of the hydrogen-bond interactions of the substrate OH groups with protein functional groups similar to the related enzyme transaldolase that also acts on phosphoketoses[34,35]. This rationalizes the known high specificity of TKs toward substrates with 1-OH groups over related 2-keto compounds like pyruvate, as the multistep substrate binding leads to a coupled and hence efficient 'proofreading' of the substrate. This poses a severe challenge for the biocatalytically important redesign of the substrate specificity of TKs, as multiple reactant and transition states need be reconfigured simultaneously.

The observed configuration of the pre-reaction state would also ensure an efficient reactant separation between the thiamine cofactor and the substrate. A near-attack[36] configuration could potentially result in a non-productive state that is too stable, since the sugar substrates could never 'escape' the covalent reaction with the cofactor thiazolium (recombination with carbanion/carbene)[18] and would thus be trapped at the active site, a situation that is similar to the avoidance of the internal return of CO_2 in decarboxylases[37]. The non-covalently bound substrate in the pre-reaction state is not yet distorted or otherwise stressed as previously reported for the covalent substrate–thiamine conjugate. This underscores the notion that the thermodynamic cost required to distort the physical substrate is paid in large part by the enthalpy of carbonyl addition of the substrate to the cofactor carbene as observed for thiamine enzymes[26]; accordingly, the same scenario might apply to the formation of distorted covalent intermediates in Schiff-base-forming enzymes and flavoenzymes[34,38]. This observation is in line with the proposal that non-covalently bound substrates are unlikely to be severely strained in enzymes, since the protein fold itself is too flexible to exert stress[39]. Nonetheless, distorted intermediates were observed for enzymes not involving covalent catalysis; however, the catalytic contribution of strain in this system was found to be small[40].

Apart from the implications for fundamental aspects of enzyme catalysis, our findings are promising in the context of developing new antibiotics. The observation of selective inhibition of *E. coli* targets compared with the human homologs (Supplementary Table 3) may prove useful when exploring the feasibility of MTh, or related precursors with modifications of the thiamine scaffold, as antibiotics. As human ThDP enzymes are apparently able to either discriminate between ThDP and MThDP (*Hs*TK and human oxoglutarate dehydrogenase) or retain enzymatic activity with MThDP (*Hs*PDH), ThDP deficiency is unlikely to result from treatment with MTh. It is difficult to predict at this point if and by which mechanisms bacteria might develop resistance against MTh, in particular because the major in vivo targets need to be identified, for example, by cellular thermal shift assays, as reported for other drug targets[41,42].

In summary, here we disentangled the modus operandi of the toxic thiamine antivitamin MTh. Our experimental and computational analyses revealed a differential effect of this antivitamin on human and bacterial enzyme targets, demonstrating the potential of this antivitamin and related compounds for antibiotic treatment. In a broader context, our findings may prove useful for devising strategies to develop antibiotics from naturally occurring or synthetic antivitamins, which might at first seem counterintuitive in view of the vital roles of vitamins and a putative interference of the corresponding antivitamins. However, as shown here, nature has evolved enzyme systems that can effectively discriminate between structurally similar compounds that differ in only one additional atom, thus qualifying cofactor-bearing enzymes as 'druggable targets', provided the human and bacterial orthologs are sufficiently different in the cofactor-binding locale to discriminate between vitamin and antivitamin.

Online content

Any methods, additional references, Nature Research reporting summaries, source data, extended data, supplementary information, acknowledgements, peer review information; details of author contributions and competing interests; and statements of data and code availability are available at https://doi.org/10.1038/s41589-020-0628-4.

Received: 9 December 2019; Accepted: 17 July 2020;
Published online: 24 August 2020

References

1. Alanis, A. J. Resistance to antibiotics: are we in the post-antibiotic era? *Arch. Med. Res.* **36**, 697–705 (2005).
2. Kohansky, M. A., Dwyer, D. J. & Collins, J. J. How antibiotics kill bacteria: from targets to networks. *Nat. Rev. Microbiol.* **8**, 423–435 (2010).
3. Otani, S., Takatsu, M., Nakano, M., Kasai, S. & Miura, R. Letter: roseoflavin, a new antimicrobial pigment from *Streptomyces*. *J. Antibiot.* **27**, 86–87 (1974).

4. Wada, K. & Haga, M. *Ginkgo Biloba—A Global Treasure* (eds. Hori, T. et al.) 309–321 (Springer Japan, 1997).
5. Drautz, H., Messerer, W., Zähner, H., Breiding-Mack, S. & Zeeck, A. Metabolic products of microorganisms. 239. Bacimethrin isolated from *Streptomyces albus* identification, derivatives, synthesis and biological properties. *J. Antibiot.* **40**, 1431–1439 (1987).
6. Reddick, J. J. et al. The mechanism of action of bacimethrin, a naturally occurring thiamin antimetabolite. *Bioorg. Med. Chem. Lett.* **11**, 2245–2248 (2001).
7. Pedrolli, D. B. et al. The antibiotics roseoflavin and 8-demethyl-8-amino-riboflavin from *Streptomyces davawensis* are metabolized by human flavokinase and human FAD synthetase. *Biochem. Pharmacol.* **82**, 1853–1859 (2011).
8. Leistner, E. & Drewke, C. Ginkgo biloba and ginkgotoxin. *J. Nat. Prod.* **73**, 86–92 (2010).
9. Lee, E. R., Blount, K. F. & Breaker, R. R. Roseoflavin is a natural antibacterial compound that binds to FMN riboswitches and regulates gene expression. *RNA Biol.* **6**, 187–194 (2009).
10. Langer, S., Hashimoto, M., Hobl, B., Mathes, T. & Mack, M. Flavoproteins are potential targets for the antibiotic roseoflavin in *Escherichia coli*. *J. Bacteriol.* **195**, 4037–4045 (2013).
11. Nemeria, N. S. et al. Competence of thiamin diphosphate-dependent enzymes with 2′-methoxythiamin diphosphate derived from bacimethrin, a naturally occurring thiamin antivitamin. *Biochemistry* **55**, 1135–1148 (2016).
12. Schneider, G. & Lindqvist, Y. Crystallography and mutagenesis of transketolase: mechanistic implications for enzymatic thiamin catalysis. *Biochim. Biophys. Acta* **1385**, 387–398 (1998).
13. Tittmann, K. Sweet siblings with different faces: the mechanisms of FBP and F6P aldolase, transaldolase, transketolase and phosphoketolase revisited in light of recent structural data. *Bioorg. Chem.* **57**, 263–280 (2014).
14. Dai, S. et al. Low-barrier hydrogen bonds in enzyme cooperativity. *Nature* **573**, 609–613 (2019).
15. Frank, R. A., Titman, C. M., Pratap, J. V., Luisi, B. F. & Perham, R. N. A molecular switch and proton wire synchronize the active sites in thiamine enzymes. *Science* **306**, 872–876 (2004).
16. Kern, D. et al. How thiamine diphosphate is activated in enzymes. *Science* **275**, 67–70 (1997).
17. Asztalos, P. et al. Strain and near attack conformers in enzymic thiamin catalysis: X-ray crystallographic snapshots of bacterial transketolase in covalent complex with donor ketoses xylulose 5-phosphate and fructose 6-phosphate, and in noncovalent complex with acceptor aldose ribose 5-phosphate. *Biochemistry* **46**, 12037–12052 (2007).
18. Meyer, D., Neumann, P., Ficner, R. & Tittmann, K. Observation of a stable carbene at the active site of a thiamin enzyme. *Nat. Chem. Biol.* **9**, 488–490 (2013).
19. Nemeria, N. S., Chakraborty, S., Balakrishnan, A. & Jordan, F. Reaction mechanisms of thiamin diphosphate enzymes: defining states of ionization and tautomerization of the cofactor at individual steps. *FEBS J.* **276**, 2432–2446 (2009).
20. Paulikat, M., Wechsler, C., Tittmann, K. & Mata, R. A. Theoretical studies of the electronic absorption spectra of thiamin diphosphate in pyruvate decarboxylase. *Biochemistry* **56**, 1854–1864 (2017).
21. Tittmann, K. et al. NMR analysis of covalent intermediates in thiamin diphosphate enzymes. *Biochemistry* **42**, 7885–7891 (2003).
22. Kluger, R. & Tittmann, K. Thiamin diphosphate catalysis: enzymic and nonenzymic covalent intermediates. *Chem. Rev.* **108**, 1797–1833 (2008).
23. Muller, Y. A. et al. A thiamin diphosphate binding fold revealed by comparison of the crystal structures of transketolase, pyruvate oxidase and pyruvate decarboxylase. *Structure* **1**, 95–103 (1993).
24. Kaplun, A. et al. Glyoxylate carboligase lacks the canonical active site glutamate of thiamine-dependent enzymes. *Nat. Chem. Biol.* **4**, 113–118 (2008).
25. Burgi, H. B., Dunitz, J. D., Lehn, J. M. & Wipff, G. Stereochemistry of reaction paths at carbonyl centers. *Tetrahedron* **30**, 1563–1572 (1974).
26. Lüdtke, S. et al. Sub-ångström-resolution crystallography reveals physical distortions that enhance reactivity of a covalent enzymatic intermediate. *Nat. Chem.* **5**, 762–767 (2013).
27. Neumann, P. & Tittmann, K. Marvels of enzyme catalysis at true atomic resolution: distortions, bond elongations, hidden flips, protonation states and atom identities. *Curr. Opin. Struct. Biol.* **29**, 122–133 (2014).
28. Booth, C. K. & Nixon, P. F. Reconstitution of holotransketolase is by a thiamin-diphosphate-magnesium complex. *Eur. J. Biochem.* **218**, 261–265 (1993).
29. Mitschke, L. et al. The crystal structure of human transketolase and new insights into its mode of action. *J. Biol. Chem.* **285**, 31559–31570 (2010).
30. Ciszak, E. M., Korotchkina, L. G., Dominiak, P. M., Sidhu, S. & Patel, M. S. Structural basis for flip-flop action of thiamin pyrophosphate-dependent enzymes revealed by human pyruvate dehydrogenase. *J. Biol. Chem.* **278**, 21240–21246 (2003).
31. Jarzynski, C. Equilibrium free-energy differences from nonequilibrium measurements: a master-equation approach. *Phys. Rev. E* **56**, 5018–5035 (1997).
32. Warshel, A., Papazyan, A. & Kollman, P. A. On low-barrier hydrogen bonds and enzyme catalysis. *Science* **269**, 102–106 (1995).
33. Warshel, A. & Papazyan, A. Energy considerations show that low-barrier hydrogen bonds do not offer a catalytic advantage over ordinary hydrogen bonds. *Proc. Natl Acad. Sci. USA* **93**, 13665–13670 (1996).
34. Lehwess-Litzmann, A. et al. Twisted Schiff base intermediates and substrate locale revise transaldolase mechanism. *Nat. Chem. Biol.* **7**, 678–684 (2011).
35. Light, S. H., Minasov, G., Duban, M. E. & Anderson, W. F. Adherence to Burgi–Dunitz stereochemical principles requires significant structural rearrangements in Schiff-base formation: insights from transaldolase complexes. *Acta Crystallogr. D Biol. Crystallogr.* **70**, 544–552 (2014).
36. Hur, S. & Bruice, T. C. The near attack conformation approach to the study of the chorismate to prephenate reaction. *Proc. Natl Acad. Sci. USA* **100**, 12015–12020 (2003).
37. Kluger, R. Catalyzing decarboxylation by taming carbon dioxide. *Pure Appl. Chem.* **87**, 353–360 (2015).
38. Bailey, S. S. et al. Enzymatic control of cycloadduct conformation ensures reversible 1,3-dipolar cycloaddition in a prFMN-dependent decarboxylase. *Nat. Chem.* **11**, 1049–1057 (2019).
39. Fersht, A. *Structure and Mechanism in Protein Science* (W.H. Freeman and Company, 1999).
40. Fujihashi, M. et al. Substrate distortion contributes to the catalysis of orotidine 5'-monophosphate decarboxylase. *J. Am. Chem. Soc.* **135**, 17432–17443 (2013).
41. Jafari, R. et al. The cellular thermal shift assay for evaluating drug target interactions in cells. *Nat. Protoc.* **9**, 2100–2122 (2014).
42. Begley, T. The mechanistic enzymology of thiamin biosynthesis. *FASEB J.* 29, (2015).

Methods

Synthesis of MThDP. MThDP was chemoenzymatically synthesized as detailed previously[11].

Protein expression and purification. Expression and purification of *Ec*TK was carried out as described before[17]. The holoenzyme was generated by incubation of the as-isolated apoenzyme with 500 µM of either ThDP or MThDP and 2.5 mM $CaCl_2$ for at least 1 h on ice. *Hs*TK was expressed and purified as holoenzyme as detailed previously[29]. *Hs*TK apoenzyme was prepared by acidic ammonium sulfate precipitation[26]. For recombination of *Hs*TK apoenzyme with either ThDP or MThDP, a solution of 2 mg ml^{-1} of TK apoenzyme (in 50 mM glycylglycine (GlyGly), pH 7.9, 2% glycerol) was mixed with 5 mM $CaCl_2$, 100 µM ThDP or 100 µM MThDP. Incubation was allowed to proceed on ice for 20 h.

Protein crystallization and structure determination. Crystals of *Ec*TK (in 50 mM GlyGly, 0.5 mM MThDP, 10 mM $CaCl_2$, pH 7.9) were grown using the hanging drop vapor-diffusion method, using 6-µl drops (3 µl + 3 µl mixing) against 500 µl of 19–24% (wt/vol) PEG 6000, 2% (vol/vol) glycerol and 50 mM GlyGly (pH 7.9) reservoir solution. Microseeding was carried out after 24 h. For cryoprotection, a solution consisting of 20% (wt/vol) PEG 6000 and 30% (vol/vol) ethylene glycol was used. For the soaking experiments with substrate, the solution was supplemented with 100 mM of pH-adjusted donor ketose X5P, and the crystals were incubated for 1 min in the soaking solution before flash cooling and eventual storage in liquid nitrogen.

X-ray datasets of single crystals (*Ec*TK reconstituted with MThDP and Ca^{2+}, *Ec*TK reconstituted with MThDP and Ca^{2+} and additionally soaked with X5P; see above) were collected at the European Molecular Biology Laboratory (EMBL) beamline P14 at the Deutsches Elektronen-Synchrotron (DESY) at a wavelength of 1 Å. Processing was performed using the XDS package[43]. Rigid-body phasing using the deposited structure 2R8O, model building and refinement were performed using the CCP4 and PHENIX software suites as reported before[17,44,45]. Structure validation was performed using MolProbity[46]. The MolProbity statistics for the geometry of the final models were: 98.26% favored, 1.74% allowed and 0% outliers for the structure of *Ec*TK in complex with MThDP (6TJ8); and 98.19% favored, 1.81% allowed and 0% outliers for the structure of *Ec*TK in complex with MThDP and substrate X5P (6TJ9).

Activity assay. The activity assay for EcTK-catalyzed conversion of physiological substrates

$$\mathrm{X5P} + \mathrm{R5P} \rightarrow \mathrm{G3P} + \mathrm{S7P}$$

was performed using a continuous coupled spectrophotometric assay that monitors NADH consumption as previously described, using 500 µM ThDP or MThDP and 2.5 mM $CaCl_2$ (ref. [17]). The concentration of acceptor R5P was kept constant at 5 mM, while that of donor X5P varied between 0 mM and 6 mM. Data were analyzed with the Michaelis–Menten equation (1) and the Hill equation (2).

$$v(S) = \frac{V_{\max} \times [S]}{K_{\mathrm{m}}^{\mathrm{app}} \times [S]} \quad (1)$$

$$v(S) = \frac{V_{\max} \times [S]^n}{K_{0.5}^n \times [S]^n} \quad (2)$$

For the determination of the cofactor dissociation constant $K_{\mathrm{M}}^{\mathrm{app}}$ under steady-state turnover conditions, X5P (0.75 mM) and R5P (5 mM) were kept constant, and protein pre-incubated with 0.05–20 µM ThDP or 0.2–50 µM MThDP was then added to start the reaction. Identical cofactor concentrations were adjusted for the corresponding assay mixtures. Data were analyzed with the Michaelis–Menten equation and the Hill equation (see above).

For *Hs*TK, enzymatic activities were determined as described above for *Ec*TK but using final concentrations of 300 µM X5P and 5 mM R5P in 50 mM GlyGly buffer (pH 7.6). No additional cofactors were added to the reaction mix, resulting in final concentrations of 5 µM ThDP or MThDP and 250 µM $CaCl_2$ at an enzyme concentration of 1.4 µM. The activity of as-isolated *Hs*TK holoenzyme was also assessed in the presence of 100 µM MThDP.

Reconstitution of *Hs*TK apoenzyme was kinetically analyzed at final concentrations of 400 µM X5P, 5 mM R5P, with either 100 µM ThDP or an equimolar ratio of ThDP and MThDP (100 µM), along with 5 mM $CaCl_2$.

Fluorescence spectrometry. Equilibrium binding dissociation constants (K_{D}) for ThDP and MThDP were further determined by fluorescence spectrometry for monitoring protein fluorescence quenching upon cofactor binding. Samples were excited at a wavelength of 295 nm, and emission spectra were recorded from 310–450 nm. The spectra were corrected for the individual contributions of buffer, protein and added cofactor, and the relative quenching at each cofactor concentration was calculated from the corrected spectra. The data thus obtained were fitted with a quadratic function described in equation (3):

$$F(\text{cofactor}) = F_0 + \frac{\Delta F_{\max}}{2 \times [\mathrm{TK}]} \times \left[([\text{cofactor}] + [\mathrm{TK}] + K_{\mathrm{D}}^{\mathrm{app}}) - \sqrt{([\text{cofactor}] + [\mathrm{TK}] + K_{\mathrm{D}}^{\mathrm{app}})^2 - 4 \times [\text{cofactor}] \times [\mathrm{TK}]} \right] \quad (3)$$

where $\Delta F_{\max}$ signifies the maximal amplitude of fluorescence quenching, [cofactor] is the concentration of ThDP or MThDP, [TK] is the concentration of *Ec*TK on a per-active-site basis and $K_{\mathrm{D}}^{\mathrm{app}}$ is the apparent equilibrium binding dissociation constant as a measure of cofactor affinity.

Nuclear magnetic resonance analysis of cofactor activation and intermediate distribution. The kinetics of cofactor activation of TK-bound ThDP or MThDP was measured by H/D exchange in D_2O buffer using chemical quench/^{1}H-NMR spectroscopy as reported before[16]. Data were fitted with a mono-exponential function to estimate k_{obs} of deuterium incorporation at C2 of the enzyme-bound cofactor.

The reactions of *Ec*TK with donor ketose substrates X5P and F6P were analyzed by an acid quench/^{1}H-NMR method as detailed previously[17,21]. The relative concentrations of the intermediates were estimated by ^{1}H-NMR spectrocopy using the C6′-H proton signals of ThDP (8.01 p.p.m.) and MThDP (8.04 p.p.m.) of chemically synthesized DHE-ThDP (7.31 p.p.m.) and of chemoenzymatically synthesized X5P-ThDP (7.35 p.p.m.) and F6P-ThDP (7.34 p.p.m.) adducts as standards. All experiments were performed at 20 °C.

MD simulations. *System setup.* The structures of the enzymes in complex with ThDP were taken from the PDB: *Ec*TK (1QGD), *Hs*TK (3MOS), *Ec*PDHc-E1 (2IEA) and HsPDHc-E1 (3EXE). Missing loop residues in 2IEA were modeled using Sphinx[47].

Starting structures of MThDP bound to the four studied enzymes were generated by superimposing the MThDP pose from the newly determined *Ec*TK structure in complex with MThDP onto the ThDP molecules. Apoenzyme structures were generated by removing the ligand atoms. Crystallographic water molecules were retained in the models. Protein protonation states were assigned at pH 7.4 using the protein preparation tool in HTMD (v1.12)[48], which relies on propka v3.1 (ref. [49]) and PDB2PQR[50]. To mimic the proton relay system experimentally observed in these enzymes[14], we forced the canonical glutamate and its adjacent, distal glutamate to be both protonated (E411 and E160 in 1QGD; E366 and E160 in 3MOS; E571 and E235 in 2IEA; and E59 and E28 in 3EXE). ThDP and MThDP were both simulated with a net charge of −2, and the metal ion anchoring the cofactor diphosphate group was modeled as a Mg^{2+} ion.

Proteins were modeled with the Amber99sb*-ILDN[51] force field and water with the TIP3P model[52]. Ligands were modeled with GAFF2 (v2.1) using AmberTools[53] and ACPYPE (v2017–01–17)[54]. Partial charges were obtained via restrained electrostatic potential calculations (ESPs). Geometry optimizations (up to ten steps) and molecular ESPs were performed using the Gaussian 09 program (D.01), both at HF/6–31 G* level of theory. ESP points were sampled according to the Merz–Kollman scheme.

The protein–ligand systems were solvated in a dodecahedral box with periodic boundary conditions and a minimum distance between the solute and the box of 12 Å. Sodium and chloride ions were added to neutralize the systems at a concentration of 0.15 M. Ions were introduced into the solvated system by random replacement of water molecules while ensuring a minimum distance of 5 Å between protein and ion atoms.

Simulations and free-energy calculations. All simulations were carried out in Gromacs 2016 (ref. [55]), and 10,000 energy minimization steps were performed using a steepest-descent algorithm. The systems were subsequently simulated for 0.1 ns in the isothermal–isobaric ensemble (NPT) with harmonic position restraints applied to all solute heavy atoms with a force constant of 1,000 kJ mol^{-1} nm^{-2}. Temperature was coupled using Langevin dynamics at 298.15 K, while pressure was coupled using the Berendsen weak-coupling algorithm with a target pressure of 1 bar[56]. The particle-mesh Ewald algorithm was used for electrostatic interactions with a real-space cutoff of 12 Å, spline order of 4, relative tolerance of 10^{-5} and Fourier spacing of 1.2 Å. The Verlet cutoff scheme with the potential-shift modifier was used with a Lennard–Jones interaction cutoff of 12 Å and a buffer tolerance of 0.005 kJ mol^{-1} ps^{-1}. All bonds were constrained using the P-LINCS algorithm. For equilibration, 1-ns simulations were then performed in the NPT ensemble with the Parrinello–Rahman pressure coupling algorithm at 1 bar and a time constant of 2 ps[57]. Production simulations of 2 ns were then performed. These equilibrium simulations were conducted with position restraints on solute heavy atoms when simulating the protein–ligand complexes.

For each free-energy calculation, ten repeated equilibrium simulations were used, so that the above described procedure was repeated ten times for each end state involved in the binding affinity change estimate ($\Delta\Delta G$; bound ThDP, unbound ThDP, bound MThDP and unbound MThDP). From each equilibrium simulation, 50 equally spaced frames were extracted as the starting configurations for the non-equilibrium part of the calculations, for a total of 500 frames. Coordinates for the hybrid ligands were built with pmx[58]. Energy minimization was performed

on the dummy atoms before equilibrating velocities with a 10-ps unrestrained simulation. Then, the non-equilibrium alchemical transformations (unrestrained) were performed over 100 ps, both in the forward (ThDP to MThDP) and reverse (MThDP to ThDP) direction. For the control simulations, in which the 2′-methoxy group was not introduced into ThDP, the forward non-equilibrium simulations were replaced by 100-ps equilibrium simulations in which ThDP was kept unmodified. Free-energy differences were estimated using Bennet's acceptance ratio (BAR)[59] as implemented in pmx[58]. Uncertainties in the ΔG values were calculated by taking the standard error of the BAR estimate from the ten independent equilibrium simulations and related non-equilibrium trajectories. Uncertainties in the final $\Delta\Delta G$ values were obtained by Gaussian error propagation.

The 500 forward non-equilibrium alchemical transformations provided 1,000 bound configurations of MThDP, given that TK and PDH are functional dimers binding two cofactors. The geometries of these configurations were analyzed to identify potential differences between the four enzymes studied, and their distributions are presented in Fig. 6.

Validation of the MD protocol. We performed alchemical free-energy calculations for five $\Delta\Delta G$ estimates for which experimental values were available (Supplementary Table 5). These calculations were performed to validate the simulation protocol and provide us with more confidence in the analysis of the results, where good agreement with experimental data were obtained.

Two protocols, differing only in the force field used, were initially tested. The first used the Amber99sb*-ILDN and GAFF (v2.1) force fields for the protein and the cofactor, while the second used Charmm36 and CGenFF (v3.0.1). These calculations were performed as is normally done, with unrestrained equilibrium simulations followed by non-equilibrium alchemical transitions[60]. However, we observed poor agreement with experimental data (Extended Data Fig. 6 and Supplementary Table 5), in particular for the affinity change in which we were most interested (ThDP to MThDP in *Ec*TK).

During the equilibrium simulations, we noticed the cofactor was not kept tightly bound to the *Ec*TK-binding pocket. We hypothesized that a combination of modeling issues and force-field defects could cause the quick unbinding of MThDP in equilibrium simulations, resulting in the underestimation of the repulsion between cofactor and binding pocket as a consequence of the introduced 2′-methoxy group. The systems simulated are in fact challenging for classical simulations, as they are characterized by a proton relay across multiple glutamate residues, water molecules and the cofactor itself[4]. This might have a role in stabilizing the enzyme–cofactor complex; however, this effect is not captured by the static nature of protonation states in classical simulations. Therefore, we decided to rely more heavily on the information from X-ray crystallography by limiting the equilibrium MD sampling to reside in the vicinity of the experimentally determined atomic position using heavy-atom restraints.

We then performed the same calculations to obtain all five $\Delta\Delta G$ values again, but using the restrained protocol. This was done to verify whether restricting the conformational space explored during the simulations could improve the result for the ThDP–MThDP transformation in *Ec*TK while leaving the results for the other four systems unaltered. It was found that restraining the equilibrium simulations in this way indeed improved the agreement to experimental binding affinities (Extended Data Fig. 6 and Supplementary Table 5). In particular, the restrained Amber calculations returned very good agreement with experimental data (r.m.s. error, 0.77 kcal mol^{-1}; Pearson correlation, 0.99). Improved estimates were also observed for the CHARMM calculations, but with overall lower performance than Amber (r.m.s. error, 1.19 kcal mol^{-1}; Pearson correlation, 0.42). Because of the above, we decided to focus on the simulations performed with restraints and the Amber force field for further analysis, as described.

Reporting Summary. Further information on research design is available in the Nature Research Reporting Summary linked to this article.

Data availability

The refined structural protein models and corresponding structure-factor amplitudes are deposited in the PDB under accession codes 6TJ8 (*Ec*TK in complex with cofactor analog MThDP) and 6TJ9 (*Ec*TK in complex with cofactor analog MThDP and substrate X5P). The structures cited in this publication (1QGD, 2R8O, 3MOS, 2IEA and 3EXE) are available under their respective PDB accession codes. Input files for the MD simulations are available as part of the Supplementary Information. All other data are available on request.

References

43. Kabsch, W. XDS. *Acta Crystallogr. D Biol. Crystallogr.* **66**, 125–132 (2010).
44. Bailey, S. The CCP4 suite—programs for protein crystallography. *Acta Crystallogr. D Biol. Crystallogr.* **50**, 760–763 (1994).
45. Adams, P. D. et al. PHENIX: a comprehensive Python-based system for macromolecular structure solution. *Acta Crystallogr. D Biol. Crystallogr.* **66**, 213–221 (2010).
46. Chen, V. B. et al. MolProbity: all-atom structure validation for macromolecular crystallography. *Acta Crystallogr. D. Biol. Crystallogr.* **66**, 12–21 (2010).
47. Marks, C. et al. Sphinx: merging knowledge-based and ab initio approaches to improve protein loop prediction. *Bioinformatics* **33**, 1346–1353 (2017).
48. Doerr, S., Harvey, M. J., Noe, F. & De Fabritiis, G. HTMD: high-throughput molecular dynamics for molecular discovery. *J. Chem. Theory Comput.* **12**, 1845–1852 (2016).
49. Olsson, M. H. M., Sondergaard, C. R., Rostkowski, M. & Jensen, J. H. PROPKA3: consistent treatment of internal and surface residues in empirical pKa predictions. *J. Chem. Theory Comput.* **7**, 525–537 (2011).
50. Dolinsky, T. J. et al. PDB2PQR: expanding and upgrading automated preparation of biomolecular structures for molecular simulations. *Nucleic Acids Res.* **35**, W522–W525 (2007).
51. Hornak, V. et al. Comparison of multiple amber force fields and development of improved protein backbone parameters. *Proteins* **65**, 712–725 (2006).
52. Jorgensen, W. L., Chandrasekhar, J., Madura, J. D., Impey, R. W. & Klein, M. L. Comparison of simple potential functions for simulating liquid water. *J. Chem. Phys.* **79**, 926–935 (1983).
53. Wang, J. M., Wolf, R. M., Caldwell, J. W., Kollman, P. A. & Case, D. A. Development and testing of a general amber force field. *J. Comput. Chem.* **25**, 1157–1174 (2004).
54. da Silva, A. & Vranken, W. ACPYPE—AnteChamber PYthon Parser interfacE. *BMC Res. Notes* **5**, 367 (2012).
55. Abraham, M. J. et al. GROMACS: high performance molecular simulations through multi-level parallelism from laptops to supercomputers. *SoftwareX* **2**, 19–25 (2015).
56. Berendsen, H. J. C., Postma, J. P. M., van Gunsteren, W. F., Dinola, A. & Haak, J. R. Molecular dynamics with coupling to an external bath. *J. Chem. Phys.* **81**, 3684–3690 (1984).
57. Parrinello, M. & Rahman, A. Polymorphic transitions in single crystals—a new molecular dynamics method. *J. Appl. Phys.* **52**, 7182–7190 (1981).
58. Gapsys, V., Michielssens, S., Seeliger, D. & de Groot, B. L. Pmx: automated protein structure and topology generation for alchemical perturbations. *J. Comput. Chem.* **36**, 348–354 (2015).
59. Shirts, M. R., Bair, E., Hooker, G. & Pande, V. S. Equilibrium free energies from nonequilibrium measurements using maximum-likelihood methods. *Phys. Rev. Lett.* **91**, 140601 (2003).
60. Aldeghi, M., Gapsys, V. & de Groot, B. L. Accurate estimation of ligand binding affinity changes upon protein mutation. *ACS Cent. Sci.* **4**, 1708–1718 (2018).

Acknowledgements

This study was supported by the Deutsche Forschungsgemeinschaft (FOR1296/TP3 to K.T.). We acknowledge access to beamline P14 at DESY/EMBL and thank G. Bourenkov and T. Schneider for local support. We thank R. Mata, M. McLeish and R. Kluger for discussion.

Author contributions

K.T. designed and coordinated the project. F.R.v.P. expressed and purified *E. coli* and human TK, crystallized proteins and determined the X-ray crystallographic protein structures supervised by K.T. F.R.v.P. and K.T. carried out functional analyses and interpreted functional and structural data. M.A. designed, performed, analyzed and interpreted the computer simulations. B.L.d.G. designed and supervised the execution of the computer simulations and interpreted their results. B.S. synthesized MThDP under the supervision of T.B. All authors discussed the project data. F.R.v.P., M.A. and K.T. wrote the paper with input from all other authors.

Competing interests

The authors declare no competing interests.

Additional information

Extended data is available for this paper at https://doi.org/10.1038/s41589-020-0628-4.

Supplementary information is available for this paper at https://doi.org/10.1038/s41589-020-0628-4.

Correspondence and requests for materials should be addressed to B.L.d. or K.T.

Reprints and permissions information is available at www.nature.com/reprints.

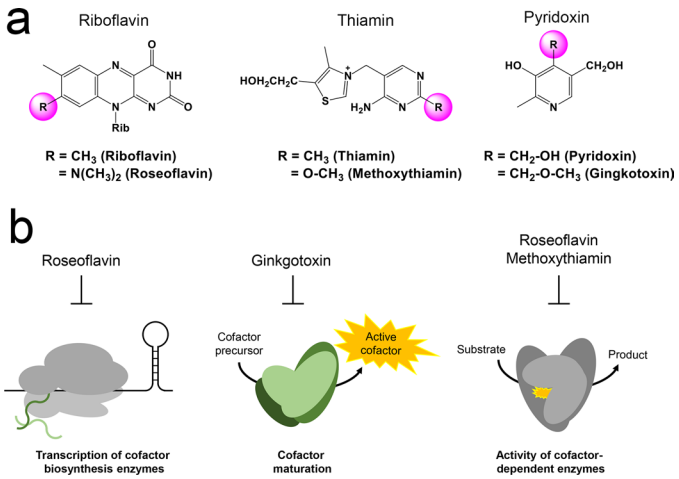

Extended Data Fig. 1 | Structure and presumed mode of action of naturally occurring vitamin B antivitamins. a, Chemical structures of vitamins B2 (riboflavin), B1 (thiamin) and B6 (pyridoxin/pyridoxal), and of corresponding antivitamins highlighting the site of modification (colored in magenta). **b**, Suggested mode of inhibition for the antivitamins shown in (**a**).

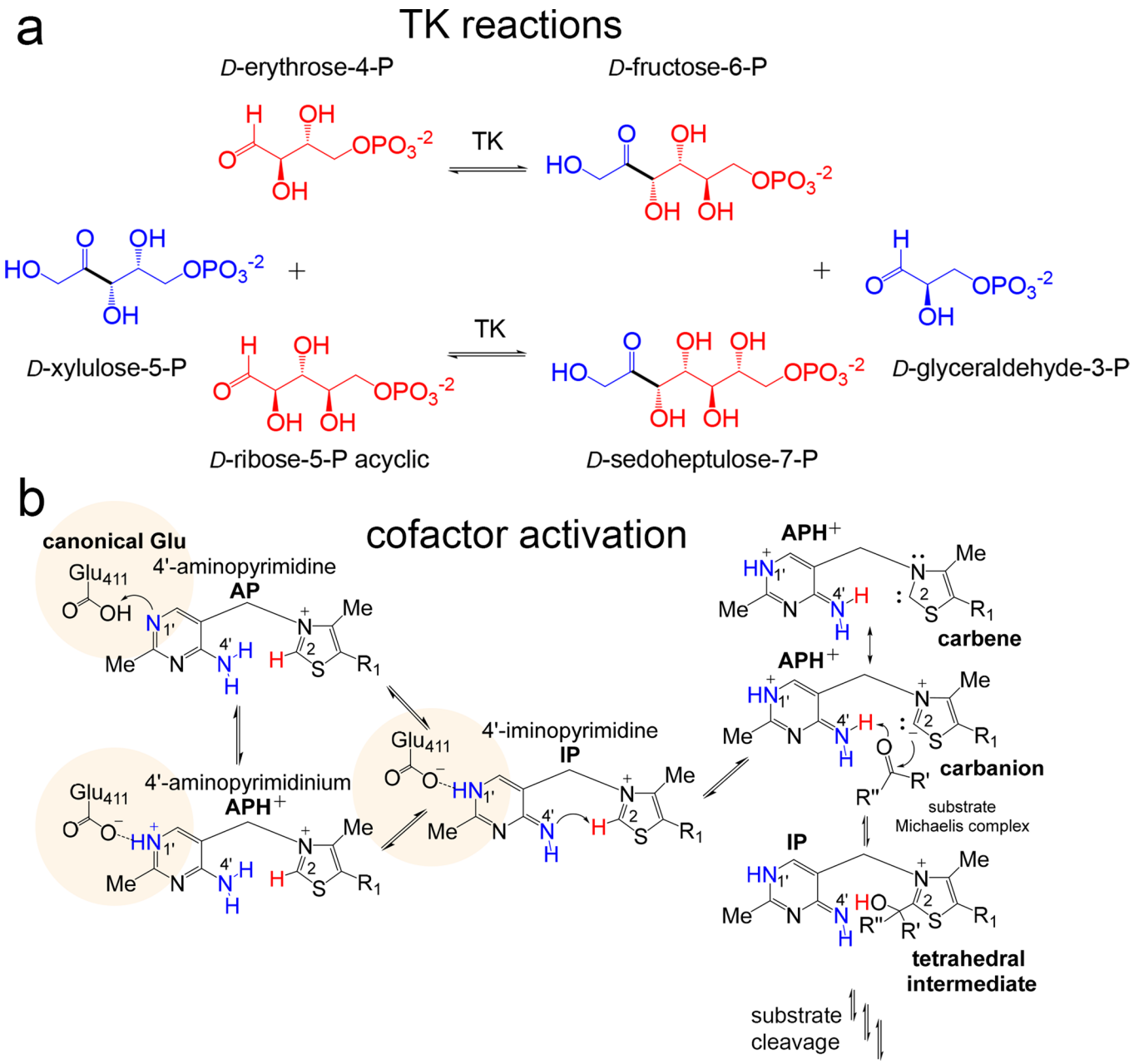

Extended Data Fig. 2 | Transketolase reactions and mechanism of cofactor activation in ThDP enzymes. a, Physiological substrates and reactions of transketolase showing the donor ketose D-xylulose-5-phosphate in blue (scissile C2-C3 bond indicated in black) and alternative aldose acceptors D-erythrose-4-phosphate and D-ribose-5-phosphate in red. **b**, Proposed mechanism of cofactor activation highlighting different cofactor protonation states and critical proton transfers. Protonation of the cofactor aminopyrimidine (AP) at atom N1′ by canonical residue E411 is thought to generate the aminopyrimidinium cation (APH⁺) form of the cofactor. Liberation of a proton from the exocyclic 4′-amino group yields the 1′,4′-iminotautomer (IP), which, owing to its high basicity, catalyses the deprotonation of the thiazolium at atom C2 (directly or via a water). The resultant carbanion/carbene nucleophilically attacks the donor substrate affording the covalent substrate-ThDP conjugate that undergoes further processing.

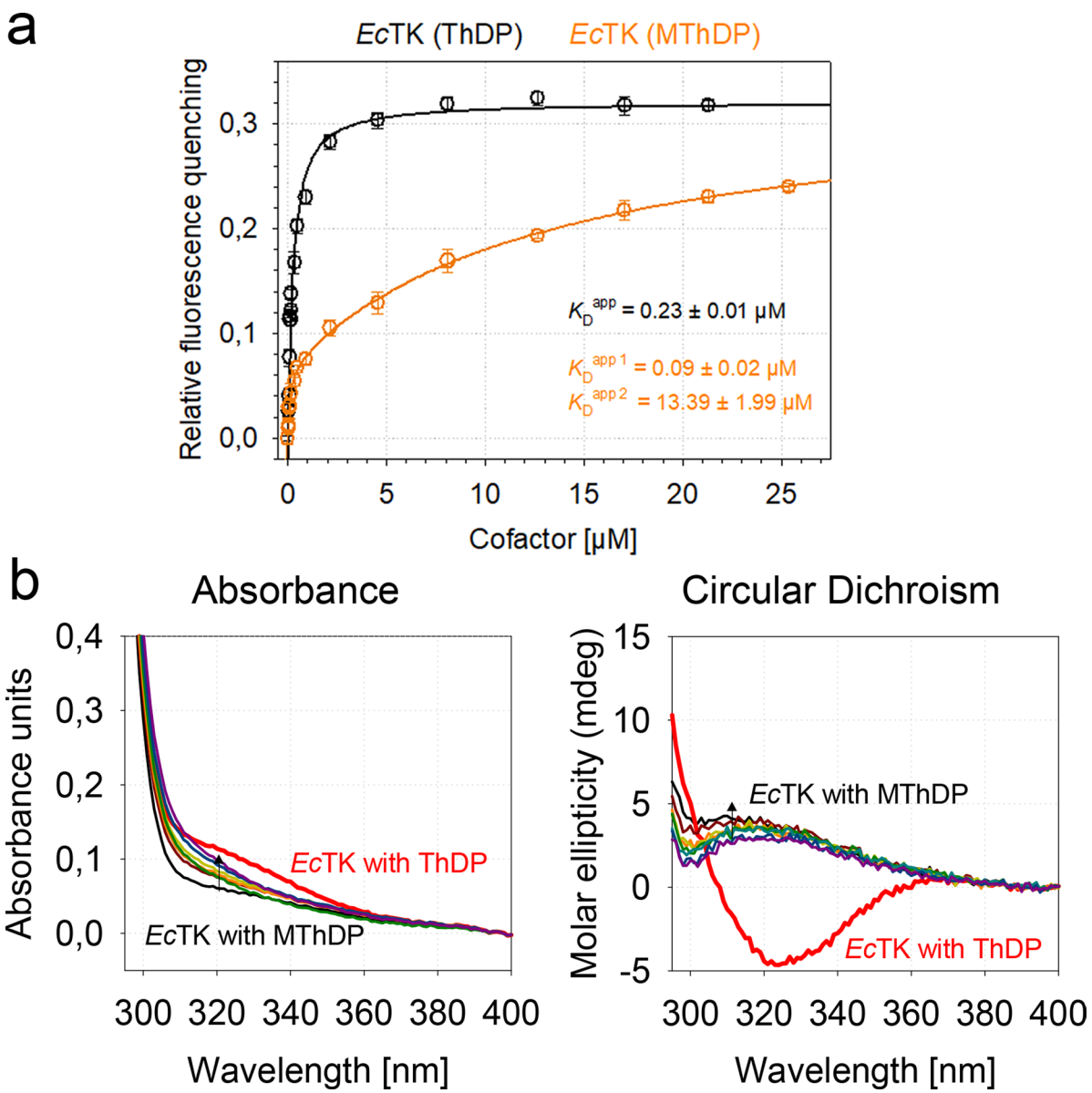

Extended Data Fig. 3 | Spectroscopic analysis of cofactor binding to *E. coli* transketolase. a, Quantitative analysis of cofactor binding to *E. coli* transketolase using genuine ThDP (black) and MThDP (orange) and monitoring fluorescence quenching of the protein. Experimental conditions are detailed in the *Methods* section. In case of ThDP, data were fitted with a quadratic function and yielded an apparent equilibrium binding constant of $K_D^{app} = 0.23 \pm 0.01\,\mu M$. For MThDP, an equation with two quadratic terms was used for fitting the data as we observed a high-affinity binding regime ($K_D^{app\,1} = 0.09 \pm 0.02\,\mu M$; 20% amplitude) and a medium-affinity binding regime ($K_D^{app\,2} = 13.39 \pm 1.99\,\mu M$; 80% amplitude). All measurements were carried out in triplicate and are shown as mean ± s.d. **b**, Absorbance and near-UV circular dichroism (CD) spectra of E. coli transketolase reconstituted with either genuine ThDP at saturating concentration (red spectra) or MThDP at increasing concentrations (0–150 μM, colored spectra). Experimental conditions are detailed in the *Methods* section. Note the prominent CD signal with a negative signature at ~325 nm for *Ec*TK in complex with ThDP that is absent for the enzyme complex with MThDP implying a different binding mode of MThDP. All experiments were independently repeated twice with similar results.

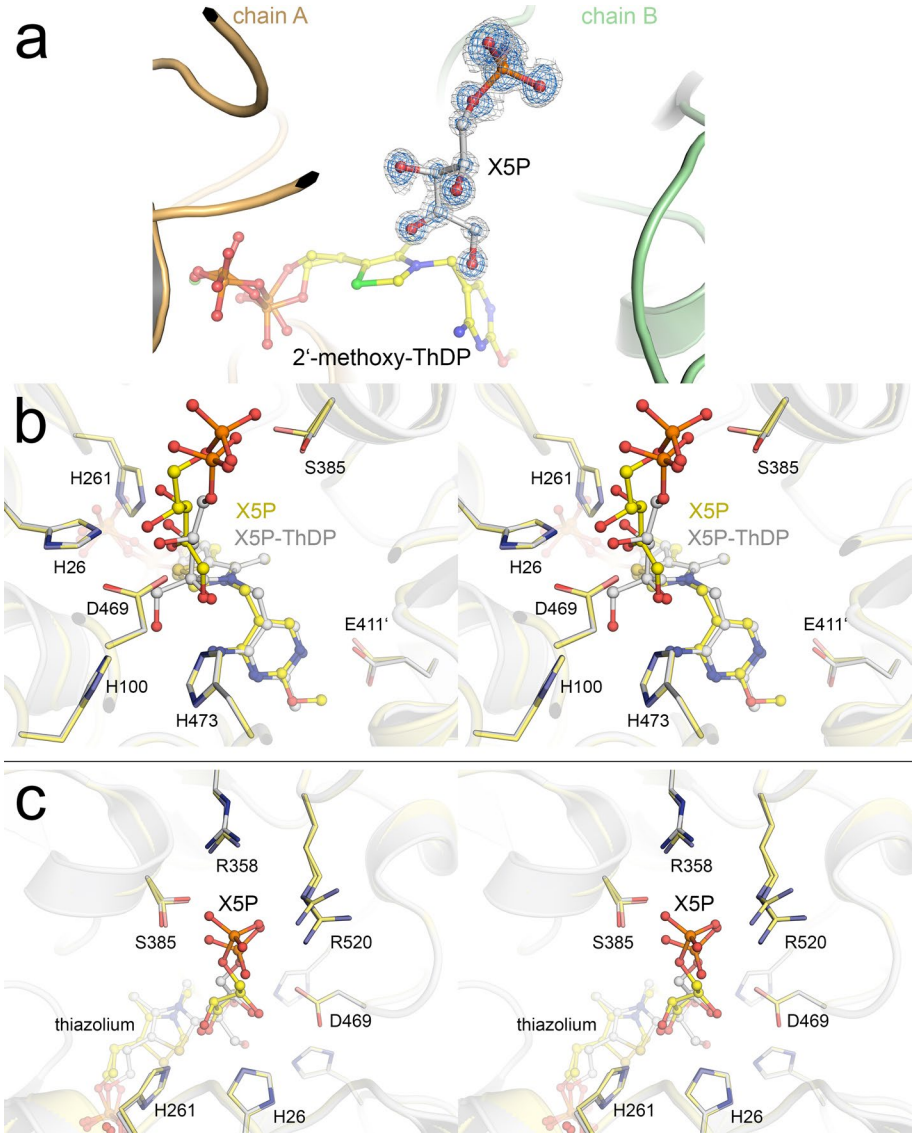

Extended Data Fig. 4 | SA omit electron density maps for substrate X5P and structural superposition of *E. coli* transketolase in non-covalent versus covalent complex with X5P. a, Simulated-annealing mFo-DFc omit electron density maps of substrate X5P noncovalently bound to *E. coli* transketolase reconstituted with 2'-methoxy-ThDP (MThDP). Omit maps are shown at contour levels of 7σ (in blue) and 4σ (in grey). The two chains of the homodimer (chain A and B) are colored individually. Simulated annealing omit maps were generated after omitting substrate X5P from the structural model. Five cycles of PHENIX.REFINE[45] were run applying cartesian simulated annealing in cycles 2 and 4, with a start temperature of 5000 K and an end temperature of 300 K. **b**, Superposition of the active site of *E. coli* transketolase in noncovalent (in yellow, this study) and covalent complex with substrate X5P (in grey, pdb code 2R8O) in stereo view showing the MThDP cofactor, substrate X5P, the covalent X5P-ThDP conjugate and selected protein groups. The active sites are shown from two different perspectives (top panel: side view; bottom panel: viewed down the substrate channel).

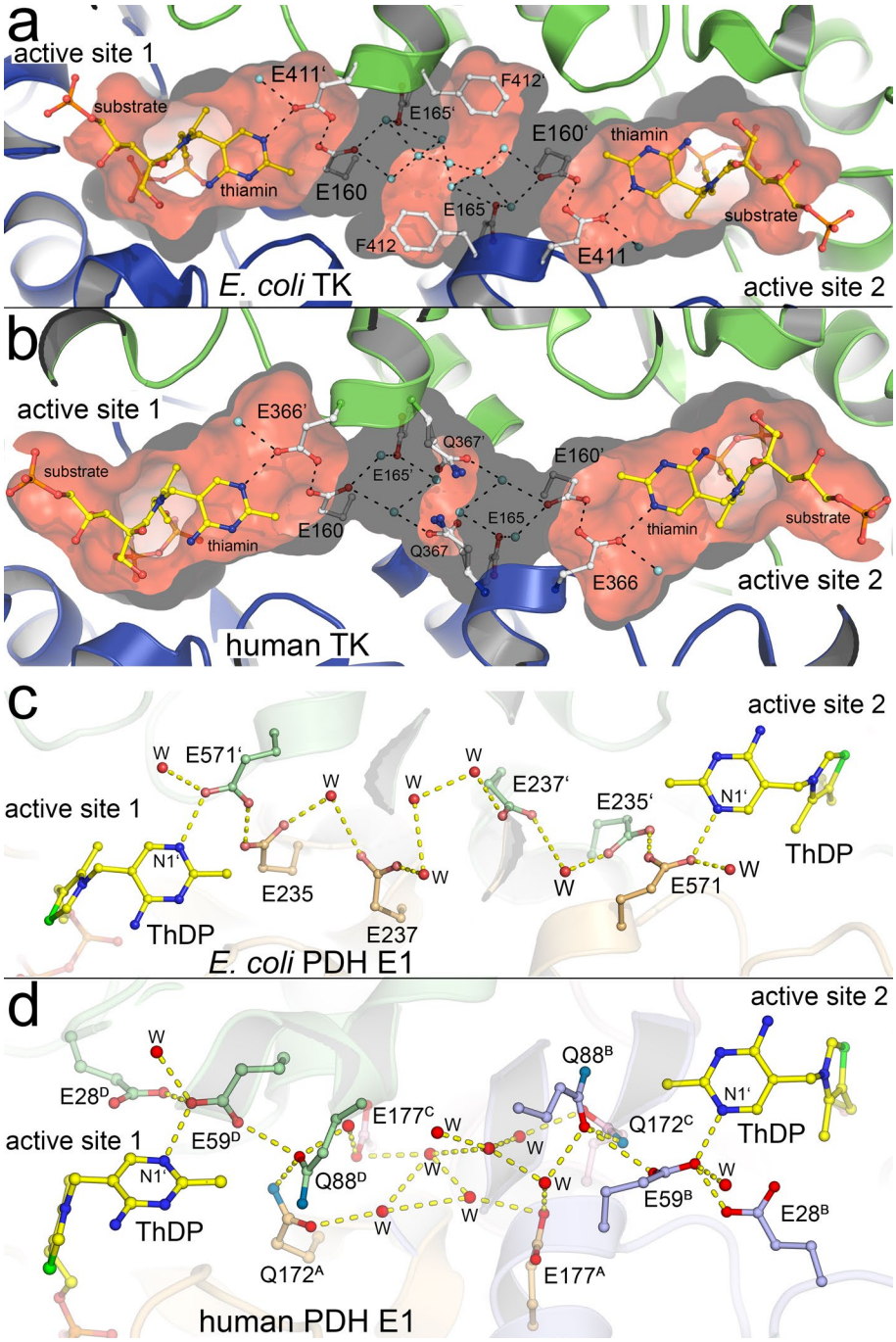

Extended Data Fig. 5 | Structures of cooperativity proton wires linking the two remote active sites in transketolases and pyruvate dehydrogenases. **a**, **b**, Structure of the cooperativity proton wire in *E. coli* (top) and human (bottom) transketolase showing selected amino acid residues, the substrate-ThDP intermediates and water molecules (pdb codes 2R8O & 4KXW). Hydrogen-bonding interactions are highlighted with dashed lines. Note that the wire architecture is highly conserved in both enzymes and consists of 6 glutamate residues and bridging water molecules (cyan spheres) providing a direct proton transfer pathway. **c**, **d**, Structure of the cooperativity communication channel in *E. coli* (top) and human (bottom) PDH E1 showing selected amino acid residues, the substrate-ThDP intermediates and water molecules (pdb codes 2IEA & 3EXE). Hydrogen-bonding interactions are highlighted with dashed lines. Note that the wire architecture in *E. coli* PDH is similar to the ones in *E. coli* and human transketolase, and consists of in total 6 glutamate residues and bridging water molecules providing a direct proton transfer pathway. In contrast, the putative communciation channel in human PDH features glutamines ($Q172^{A}$, $Q172^{C}$) that replace a critical wire glutamate (E235 in *E. coli* PDH) thus argueing against a direct proton transfer pathway.

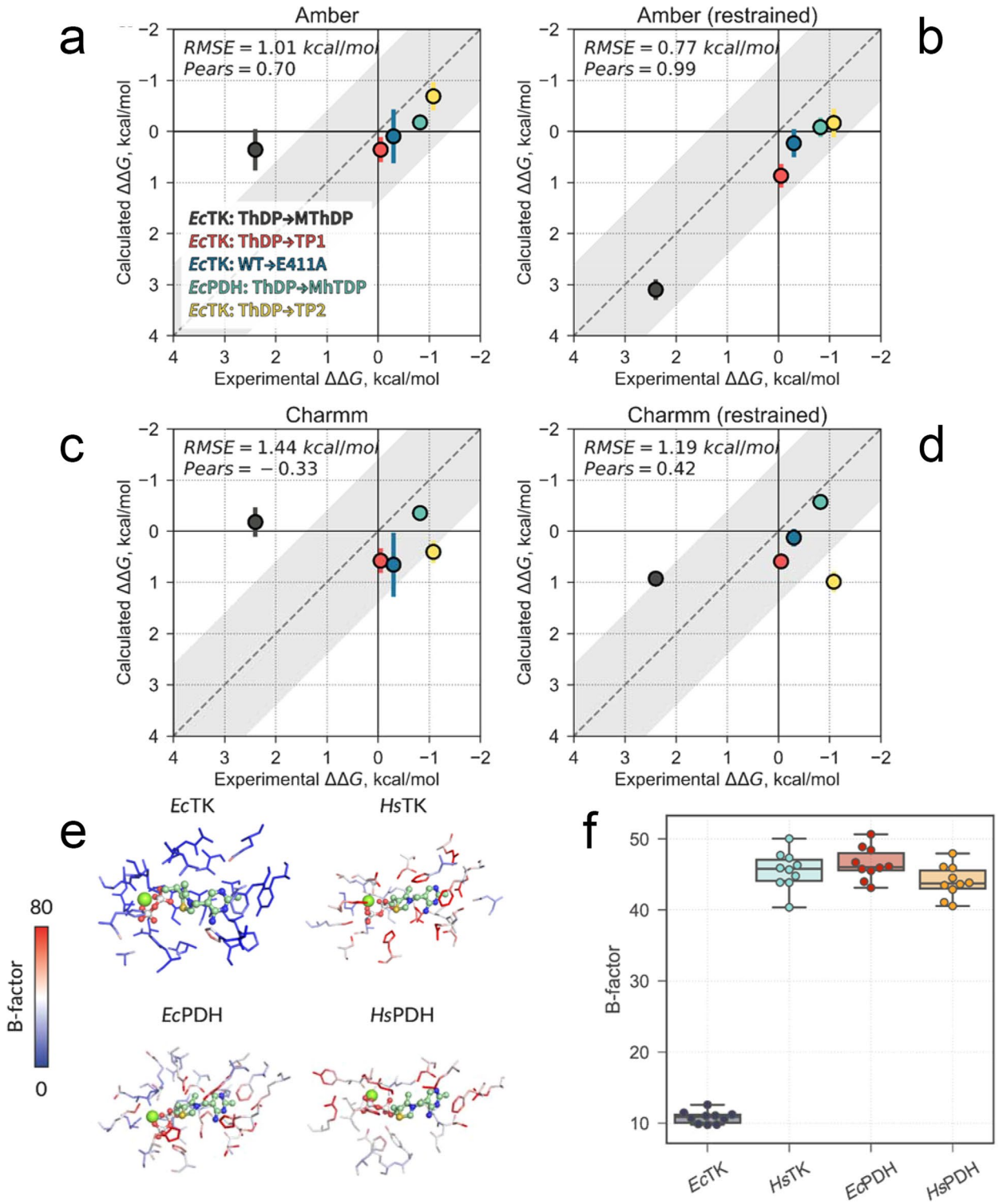

Extended Data Fig. 6 | Molecular dynamics analysis of cofactor binding in ThDP enzymes. a–d, Scatter plots of the binding free energy calculations. The Amber99sb*-ILDN/GAFF(v2.1) force field is referred to as "Amber", and the Charmm36/CGenFF(v3.0.1) force files is referred to as "Charmm". The mean and 95% confidence intervals of the calculated ΔΔG values are shown based on n = 10 independent calculations. ThDP: thiamine diphosphate; MThDP: methoxythiamin diphosphate; TP1: 4′-desamino ThDP; TP2: N3′-pyridyl ThDP; WT: wild-type; RMSE: root-mean-square error. **e**,**f**, Computed isotropic B-factors from molecular dynamics simulations. **e**, Binding pocket plasticity. The ThDP ligand is shown as green ball and sticks, and the residues within 5 Å distance are shown as sticks and color-coded according to their atomic B-factors. The Mg^{2+} ion is shown as a larger green sphere. B-factors were derived from the protein heavy-atom RMSFs, which were calculated using the final snapshots of the 500 short non-equilibrium trajectories performed with the Amber force field, as described in the main text (PDB-ID 1QGD for *E. coli* TK; PDB-ID 3MOS for human TK; PDB-ID 2IEA for E. coli PDH; PDB-ID 3EXE for human PDH). **f**, Distribution of the average binding pocket B-factors for the four complexes studied. The average RMSF for each of n = 10 independent simulations is shown as a swarmplot. The box plots are derived from these n = 10 average RMSF values. The centres of the boxes indicate the median, the bounds of the boxes indicate the first and third quartiles of the distributions, and the whiskers extend to samples up to 1.5 of the interquartile range. Samples outside the marked extrema are classified as potential outliers. Overall, the data shown in **e** and **f** suggest a higher plasticity for the binding pockets of *Hs*TK, *Ec*PDH, and *Hs*PDH than for that of *Ec*TK.

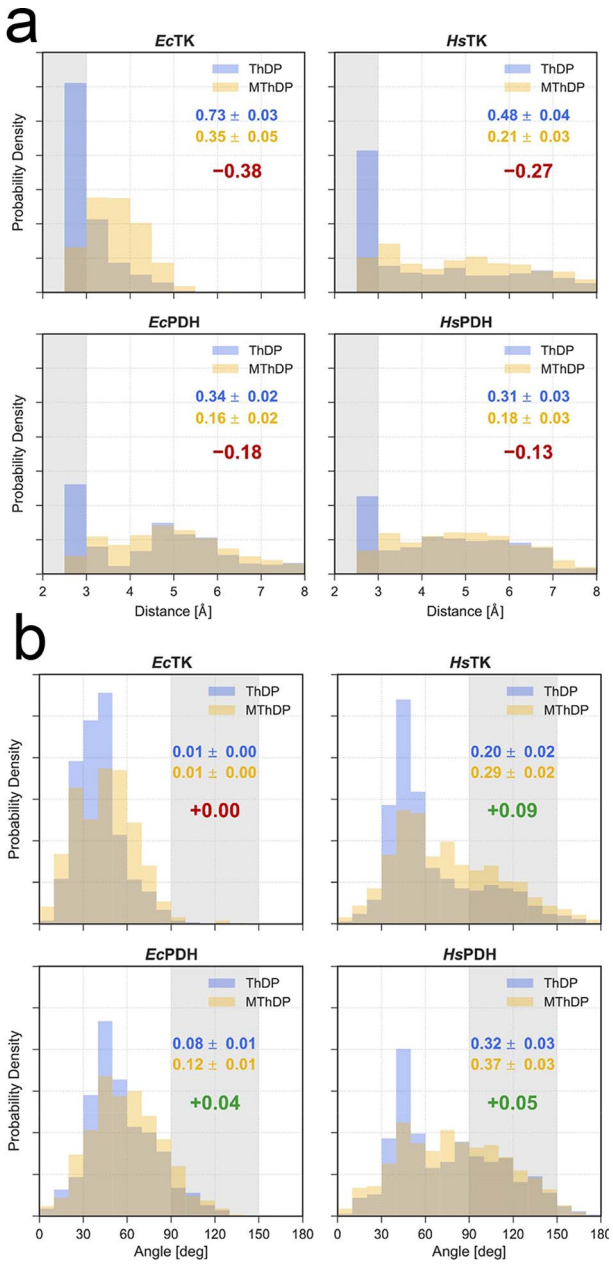

Extended Data Figure 7 | Distributions of proton donor-acceptor distances and angles for enzyme-bound ThDP and MThDP. a, Distributions of proton donor-acceptor distances for enzyme-bound ThDP and MThDP in *Ec*TK, *Hs*TK, *Ec*PDH, and *Hs*PDH. The donor is the oxygen atom on the canonical, cofactor activating glutamic acid, and the acceptor is the N1′ atom on the aminopyrimidine ring of ThDP and MThDP. The area of the plots, where the distance is in the favourable regime <3 Å is highlighted in grey. The fraction of simulation frames in which the distance was <3 Å is reported for both ThDP and MThDP; the fraction difference between MThDP and ThDP is also reported (number highlighted in red). A negative difference means that MThDP has a smaller fraction of frames with distances <3 Å. **b**, Distributions of proton donor-acceptor angles for enzyme-bound ThDP and MThDP in *Ec*TK, *Hs*TK, *Ec*PDH, and *Hs*PDH. The angle is defined between the acceptor N1′ atom in ThDP and MThDP, respectively, the donor oxygen atom on the canonial, cofactor activating glutamic acid, and the neighboring δ-carbon on the same glutamic acid. The area of the plots, where the angle is in the favourable regime between 90 and 150 degrees is highlighted in grey. The fraction of simulation frames within this area is reported for both ThDP and MThDP. The fraction difference between MThDP and ThDP is also reported. A positive difference means that MThDP has a larger fraction of frames where this angle is between 90 and 150 degrees. Note that the fractions in the favourable regime are larger for the human enzymes in complex with MThDP compared to the *E. coli* orthologs.

nature research

Corresponding author(s): Tittmann, Kai

Last updated by author(s): Jul 6, 2020

Reporting Summary

Nature Research wishes to improve the reproducibility of the work that we publish. This form provides structure for consistency and transparency in reporting. For further information on Nature Research policies, see Authors & Referees and the Editorial Policy Checklist.

Statistics

For all statistical analyses, confirm that the following items are present in the figure legend, table legend, main text, or Methods section.

n/a	Confirmed
☐	☒ The exact sample size (*n*) for each experimental group/condition, given as a discrete number and unit of measurement
☒	☐ A statement on whether measurements were taken from distinct samples or whether the same sample was measured repeatedly
☒	☐ The statistical test(s) used AND whether they are one- or two-sided *Only common tests should be described solely by name; describe more complex techniques in the Methods section.*
☒	☐ A description of all covariates tested
☒	☐ A description of any assumptions or corrections, such as tests of normality and adjustment for multiple comparisons
☐	☒ A full description of the statistical parameters including central tendency (e.g. means) or other basic estimates (e.g. regression coefficient) AND variation (e.g. standard deviation) or associated estimates of uncertainty (e.g. confidence intervals)
☒	☐ For null hypothesis testing, the test statistic (e.g. *F*, *t*, *r*) with confidence intervals, effect sizes, degrees of freedom and *P* value noted *Give P values as exact values whenever suitable.*
☒	☐ For Bayesian analysis, information on the choice of priors and Markov chain Monte Carlo settings
☒	☐ For hierarchical and complex designs, identification of the appropriate level for tests and full reporting of outcomes
☒	☐ Estimates of effect sizes (e.g. Cohen's *d*, Pearson's *r*), indicating how they were calculated

Our web collection on statistics for biologists contains articles on many of the points above.

Software and code

Policy information about availability of computer code

Data collection

Kinetics and spectroscopic analysis
Chirascan Spectrometer Control Panel Application version 4.2.27 (Circular Dichroism)
Spectra Manager version 2.07.02 (Build 4) (UV-Vis-based Kinetics)
mxCuBE 2 (X-ray data collection at DESY, Hamburg, Germany)
FluorEssence 3.5 (Fluorescence based cofactor binding)
TopSpin 3.5 (1H NMR)

Molecular Dynamics Simulations:
Gromacs 2016

Data analysis

Kinetics and spectroscopic analysis
Pro-Data Viewer version 4.2.27 (Circular Dichroism)
Spectra Manager version 2.07.02 (Build 4) (UV-Vis-based Kinetics)
SigmaPlot version 11.0 (Circular Dichroism, Stopped-Flow Kinetics, UV-Vis-based Kinetics, Fluorescence based cofactor binding)
Kaleidagraph version 4.03 (NMR)

Crystallography
XDS version Oct 15, 2015 BUILT=20151231 (X-ray, data processing)
XSCALE version May 1, 2016 BUILT=20160617 (X-ray, data scaling)
CCP4 version 6.4.0 (X-ray, processing and refinement)
phenix.refine version 1.11.1_2575 (structure, refinement)
phenix.refine version 1.13_2998 (structure, refinement)
COOT version 0.8.9.2 (structure, model building)
MolProbity-Server Version 4 (structure validation)
The PyMOL Molecular Graphics System version 1.3 (structure representation)

Molecular Dynamics Simulations:
Gromacs 2016
Python 2.7 (libraries: numpy, scipy, pmx, matplotlib, seaborn)

For manuscripts utilizing custom algorithms or software that are central to the research but not yet described in published literature, software must be made available to editors/reviewers. We strongly encourage code deposition in a community repository (e.g. GitHub). See the Nature Research guidelines for submitting code & software for further information.

Data

Policy information about availability of data

All manuscripts must include a data availability statement. This statement should provide the following information, where applicable:

- Accession codes, unique identifiers, or web links for publicly available datasets
- A list of figures that have associated raw data
- A description of any restrictions on data availability

The refined structural protein models and corresponding structure-factor amplitudes are deposited under PDB accession codes 6TJ8 (Escherichia coli transketolase in complex with cofactor analog 2'-methoxythiamine diphosphate) and 6TJ9 (Escherichia coli transketolase in complex with cofactor analog 2'-methoxythiamine diphosphate and substrate xylulose 5-phosphate). The structures cited in this publication (1QGD, 2R8O, 3MOS, 2IEA and 3EXE) are available under their respective PDB accession codes. All other data are available on request.

Field-specific reporting

Please select the one below that is the best fit for your research. If you are not sure, read the appropriate sections before making your selection.

☒ Life sciences ☐ Behavioural & social sciences ☐ Ecological, evolutionary & environmental sciences

For a reference copy of the document with all sections, see nature.com/documents/nr-reporting-summary-flat.pdf

Life sciences study design

All studies must disclose on these points even when the disclosure is negative.

Sample size	This study did not involve a sample analysis.
Data exclusions	No data were excluded.
Replication	All functional analyses were carried out as triplicates (n=3), the resulting mean +/- standard deviation are shown as error bars. Fitting of the data yielded standard errors for all estimated parameters. MD simulations: All calculations were repeated 10 times; the resulting mean and its standard error are shown as error bars.
Randomization	not applicable as this study did not involve a sample analysis.
Blinding	not applicable as this study did not involve a sample analysis.

Reporting for specific materials, systems and methods

We require information from authors about some types of materials, experimental systems and methods used in many studies. Here, indicate whether each material, system or method listed is relevant to your study. If you are not sure if a list item applies to your research, read the appropriate section before selecting a response.

Materials & experimental systems

n/a	Involved in the study
☒	☐ Antibodies
☒	☐ Eukaryotic cell lines
☒	☐ Palaeontology
☒	☐ Animals and other organisms
☒	☐ Human research participants
☒	☐ Clinical data

Methods

n/a	Involved in the study
☒	☐ ChIP-seq
☒	☐ Flow cytometry
☒	☐ MRI-based neuroimaging